Carnegie Mellon University

CARNEGIE INSTITUTE OF TECHNOLOGY

THESIS

SUBMITTED IN PARTIAL FULFILLMENT OF THE REQUIREMENTS

FOR THE DEGREE OF Doctor of Philosophy

TITLE   Quenched Stresses and Linear Elastic Response of Random

Packings of Frictionless Particles Near Jamming

PRESENTED BY   Kamran Karimi

ACCEPTED BY THE DEPARTMENTS OF

Civil and Environmental Engineering

Craig Maloney   February 25, 2014
ADVISOR, MAJOR PROFESSOR   DATE

David A. Dzombak   February 26, 2014
DEPARTMENT HEAD   DATE

APPROVED BY THE COLLEGE COUNCIL

Vijayakumar Bhagavatula   February 28, 2014
DEAN   DATE

**Quenched Stresses And Linear Elastic
Response Of Random Packings Of
Frictionless Particles Near Jamming**

Submitted in partial fulfillment of the requirements for

the degree of

Doctor of Philosophy

in

Civil And Environmental Engineering

Kamran Karimi

B.S., Civil Engineering, University of Tehran

M.S., Civil Engineering, Sharif University of Technology

Carnegie Mellon University

Pittsburgh, PA

May, 2014

Acknowledgements

If I want to make a list of people whom I need to thank, I will end up with a very long one; this list will consist of the people I have been interacting with here at CMU including my advisor, lab mates, and other faculties as well as my family and close friends in my home country. I will have to sort this list in my head – based on the help and support I received – and then decide who comes first!

I would like to thank my parents first: thank you for all the sacrifices and efforts you have made for my sake; I truly mean it. Your kindness and love were a great source of help in all these years. And, when it comes to love and support, how could I forget to mention my two lovely sisters. Inside academia, I must certainly first mention my advisor Craig Maloney to whom I owe a very big thank-you; for the encouragement and priceless advice I received from you in my research and for a new door you opened in my academic career. You have always been a great mentor to me. And very special thanks to Asad Hasan. I was very lucky that he started his Phd at CMU in the same year as I did, whose valuable comments and suggestions always improved my work. I must say I always envied your passion and love about science. You have been a great friend, lab mate, and English teacher! Certainly, there are many other names that could have been here. They are not listed but without them, I would not have been able to make progress in my academic life. I would also like to thank my committee members, Professor Bielak, Professor Khair, Professor Higgs, and Professor Maloney who chaired the committee. My dissertation work was supported through a grant from the Berkman faculty

Abstract

We study stress correlations and elastic response in large-scale computer simulations of particle packings near jamming. We show that there are characteristic lengths in both the stresses and elastic response that diverge in similar ways as the confining pressure approaches zero from above. For the case of the stress field, we show that the power spectrum of the hydrostatic pressure and shear stress agrees with a field-theoretic framework proposed by Henkes and Chakraborty [15] at short to intermediate wavelengths (where the power is flat in Fourier space), but contains significant excess power at wavelengths larger than about 50 to 100 particle diameters, with the specific crossover point going to larger wavelength at decreasing pressure, consistent with a divergence at $p = 0$. These stress correlations were missed in previous studies by other groups due to limited system size. For the case of the elastic response, we probe the system in three ways: i) point forcing, ii) *constrained* homogeneous deformation where the system is driven with no-slip boundary conditions, and iii) *free periodic* homogeneous deformation. For the point force, we see distinct characteristic lengths for longitudinal and transverse modes each of which diverges in a different way with decreasing pressure with $\xi_T \sim p^{-1/4}$ and $\xi_L \sim p^{-0.4}$ respectively. For the constrained homogeneous deformation we see a scaling of the local shear modulus with the size of the probing region consistent with $\xi \sim p^{-1/2}$ similar to the $\xi_L \sim p^{-0.4}$ observed in the longitudinal component of the point response and in perfect agreement with the rigidity length discussed in recently proposed scenarios for jamming. Finally, we show that the transverse and longitudinal contributions to

the strain field in response to unconstrained deformation (either volumetric or shear) have markedly different behavior. The transverse contribution is surprisingly invariant with respect to p with localized shear transformations dominating the response down to surprisingly small pressures. The longitudinal contribution develops a feature at small wavelength that intensifies with decreasing p but does not show any appreciable change in length. We interpret this pressure-invariant length as the characteristic shear zone size.

Contents

vii

List of Figures

x

List of Tables

Chapter 1

Introduction

Metallic glasses, foams, micro gels, emulsions, colloids, granular materials, and other so-called "soft" materials all have a common property: they are by nature discrete and disordered. Despite lacking any underlying crystalline order, densely packed amorphous systems behave like elastic solids at sufficiently small strains. The term *dense* means that each particle is in contact with several of its neighbors, and it is often related to a global confining pressure that keeps the particles in contact with each other. In repulsive systems such as emulsions, micro gel suspensions, and granular media, by releasing the confining pressure, these materials can be made to yield through applying a very small stress. The situation in which particles reconfigure themselves in such a way that the whole system start to resist against finite stress is called the *jamming transition* [24]. A similar scenario applies to glasses where temperature, instead, controls rigidity of the packing. As one might imagine, elastic properties depend on the distance to jamming, which is set by the external pressure. Measurement of disordered packings through

experiments and numerical simulations have found an elastic shear modulus that vanished as the volume fraction of particles ϕ reached a critical value ϕ_c [1, 34, 19, 36]. This scenario has been related to an abundance of low-energy *floppy* modes in weakly compressed packings near jamming [52, 53].

When it comes to describing the elastic linear response of jammed materials such as foams, emulsions or granular media, use of linear *isotropic homogeneous* elasticity theory appears very tempting. One would only need to obtain *bulk* elastic constants, from either simulations or experiments, and use them as an input in continuum modeling. Such a description implies these materials to be homogeneous and isotropic at a sufficiently large macroscopic size – which is reasonable as long as one is interested in capturing bulk properties. One of the central purposes of this thesis is to quantify limits of applicability of such continuous homogenized approaches. It has been suggested that packings can be essentially treated as an uniform elastic medium beyond a length that diverges at rigidity transition [52, 10, 11]. However, there is still a debate about the precise form of such a divergence. The present work should provide a framework for measuring this length and quantifying its divergence near the transition point.

Solid-like features observed in dense amorphous systems are in first place due to particle-level contact forces which cannot be neglected in the study of their mechanical response. Photo elastic experiments [6, 16] and numerical simulations [30, 39] revealed that internal stresses are transmitted in a quite inhomogeneous manner. The observed spatial variations in the quenched stress structure are a direct signature of inherent disorder. A statistical description is necessary on the microscopic level to quantify these fluctuations

[8, 47]. There has been a great deal of work on the statistics of contact forces with relatively little emphasis on their organization in space [25, 38]. Our study of stress correlations should shed more light on this rather incomplete subject in the literature.

In this work, we use discrete particle simulations to study large particle packings. Soft particles are modeled as two dimensional disks with a finite radius in our simulations. To avoid crystallization, large scale packings are made bidisperse [40]. Once the contact law is defined between disks, packings are generated using conjugate gradient at a prescribed area fraction. This is a commonly used model and preparation protocol [40] and should apply to various types of soft matters. Therefore, results should be applicable to micro gels, emulsions, and granular materials where frictional forces are negligible.

We work on a particle level taking into account the local stress field in static configurations. In a static packing, we associate each contact with a repulsive force, resulting in a *force network* with interesting spatial patterns of large forces. In Chapter 2, their spatial properties will be reviewed, and a novel description of stress correlations, based on the present anisotropy and heterogeneity, will be introduced. Chapter 3 will discuss the nature of linear elastic response of static disordered solids with various mechanical perturbations.

Chapter 2

Quenched Stresses

2.1 Introduction

Static amorphous solids form *force networks* in response to an external applied stress. The spatial structure of inter-particle contacts and associated mechanical forces, which form the force network in a disordered medium, has a direct impact on its mechanical response [31, 17]. An unusual feature of force patterns in these amorphous materials is presence of *force chains*, as demonstrated by means of photo elastic experiments [6, 25, 16, 12] and numerical simulations [43, 32, 41]. These studies give clear evidence that these geometrically complex structures support most of the internal stresses in the medium and make the distribution of contact forces extremely heterogeneous in space.

Despite their obvious appearance, the characterization of force chains has remained rather incomplete. There is a general agreement that the stress distribution decays above the mean in a *non* Gaussian fashion [25, 38]. Below the mean force, there is an abundance of small force values and the distribution exhibits a plateau. Another statistical quantity is the two-point force correlations [38, 28, 45] which doesn't contain any direct information about how stresses are organized in space. In [30], spatial correlations between the averaged contact forces were measured experimentally in a quasi static manner. This study demonstrated that force correlations depend sensitively on the packing preparation; while packings show short ranged correlations under isotropic compression, in sheared systems the force correlations decay slowly in the compressive directions [26]. Other approaches have focused on topological characterizations [41, 2, 18] and statistics of spatially averaged

forces [39].

Henkes and Chalkraborty (HC) [14, 15, 27] established constitutive relations for various stress components within a statistical mechanics framework. HC found a single characteristic size by performing numerical simulations and found it to be on the order of a few particle diameters in isotropically compressed samples. Beyond this length the stresses were found to be essentially uncorrelated. Our study of stress fluctuations agree with their field theory at small samples but contains significant deviation at large sizes. These stress correlations were missed in previous studies by other groups due to limited system size. Furthermore, emergence of spatial correlations in these studies was connected to the boundary stresses at a global length. In the absence of this boundary induced anisotropy, the extent of correlations have been shown to be rather localized [30, 15].

However, even in an isotropically prepared sample with a globally hydrostatic stress state, internal stresses look highly anisotropic at small scales (see Fig. 2.4). This local anisotropy appears due to strongly correlated forces along the direction of chains and vanishes globally when stress reaches its hydrostatic state. This observation allows us to define an important crossover length quantifying the size of force networks. The naive intuition is that the force chains should make the stress very anisotropic in local regions, and once one looks beyond a typical chain size, the stress anisotropy would decay very fast. A systematic measure of stress anisotropy at different scales can be utilized to measure stress correlations and at best identifies a characteristic size which is sensitive to jamming.

The remainder of this chapter is organized as follows: Section 2.3 will

6

briefly outline our model and also the numerical algorithm used to prepare static packings. In Section 2.4, standard stress correlations will be discussed. A modified correlation function will be introduced in order to take into account the inherent local anisotropy in stresses. Next, in Section 2.5, we will study fluctuations and anisotropy in the stress filed defined at various coarse-graining scales. These measurements will provide a natural definition for growing correlation lengths near the transition point. Finally, in Section 2.6, we will provide a discussion of our results.

2.2 Notation

We use the convention that Latin letters refer to particle indices. The Cartesian components of vectors and tensors are denoted by Greek indices. Bold types refer to vectors. As an example, $\mathbf{u}_i$ denotes a vector defined on the i-th particle whose Cartesian components are $u_{i\alpha}$.

2.3 Models And Simulation Protocols

We perform discrete element method [4] simulations of frictionless granular packings in a periodic, two-dimensional cell subject to an isotropic pressure. The packings consist of N particles and a well studied binary mixture [40]: $N_A/N_B = 1$, $d_A/d_B = 1.4$, d is the diameter of the species. The position of the i-th particle is described by $\mathbf{r}_i$. The particles interact via a pairwise, repulsive, central potential $U(r_{ij}) = \frac{1}{2}k_{ij}\delta_{ij}^2$ for $\delta_{ij} > 0$ and zero otherwise where k_{ij} is the spring constant, δ_{ij} is the overlap between the particles, $\delta_{ij} = d_{ij} - r_{ij}$, where $d_{ij} = \frac{1}{2}(d_i + d_j)$, r_{ij} is the distance between the particles. U can be alternatively defined as $U(s_{ij}) = \frac{1}{2}\bar{\epsilon}s_{ij}^2$ where $\bar{\epsilon} = k_{ij}d_{ij}^2$ is the energy scale, and $s_{ij} = \frac{\delta_{ij}}{d_{ij}}$ is the dimensionless overlap. We assume that all the bonds have the same $\bar{\epsilon}$ value, so the spring constant k_{ij} may vary (since d_{ij} is not constant). All results are reported in units of $\bar{\epsilon}$ and d_B.

The packings were prepared via a quench from a random initial state at *fixed* area fraction $\phi = \frac{\pi}{4}L^{-2}\sum_{i=1}^{N}d_i^2$, where L is the size of the simulation box. The dimensionless ϕ is defined as the ratio between the particles' area and the total available area. We perform energy minimization in the LAMMPS software package [42] with the implemented conjugate gradient method. The simulations were run until the force tolerance criterion was met.

Due to bidispersity the resulting relaxed structures created by molecular dynamics simulations are disordered, *i.e*, there is no long range crystalline order. These packings exhibit qualitatively different force patterns as the packing fraction ϕ is varied. For each set of packing fractions, we used

(a) $\phi = 0.85$ (b) $\phi = 0.925$
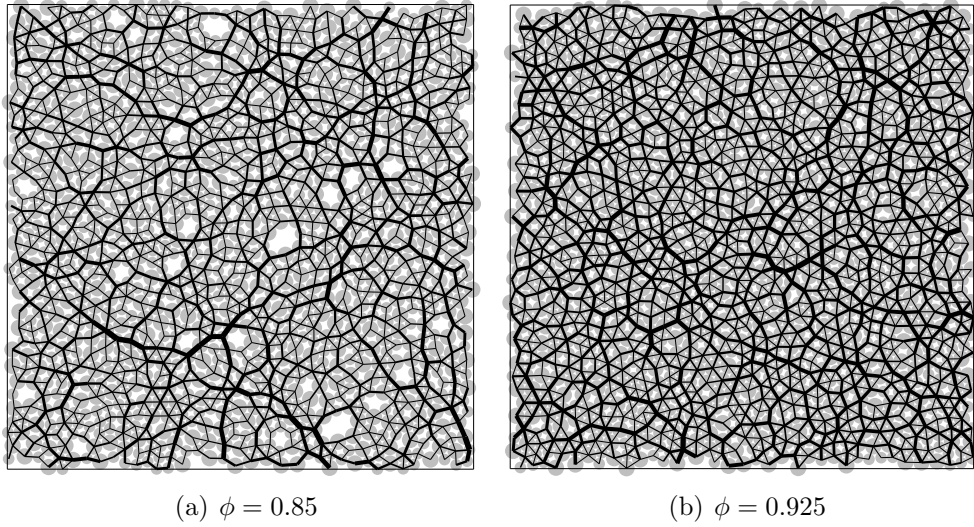
Figure 2.1: Force networks for $\phi = 0.85$ and 0.925 at $L = 320$ for a small window (40×40): The contact forces form strongly heterogeneous and anisotropic network at $\phi = 0.85$ in (a), and in (b), the network becomes more uniform in space for $\phi = 0.925$.

64 independently constructed, periodic packings with the fixed system size $L = 320$. We first considered packings at two different values of ϕ. The lower packing fraction studied, $\phi = 0.85$, leads to strongly disordered force networks with clearly visible force chains as in Fig. 2.1(a), while as the packing fraction is increased to $\phi = 0.925$, the force network becomes increasingly uniform in appearance, as shown in Fig. 2.1(b).

As usual, for a system of particles with pair-wise central forces, we define the static virial (stress *density*) for the i-th particle via the Irving-Kirkwood expression [29], $S_{\alpha\beta}(\mathbf{r}_i) = \frac{1}{2} \sum_j f_\alpha^{ij}(r_{i\beta} - r_{j\beta})$. Here, f_α^{ij} is the repulsive force vector pointing from i to j. To obtain the volumes (areas in two dimensions) occupied by each particle, the space is decomposed into cells by constructing the Voronoi diagram (see Fig. 2.2).

10
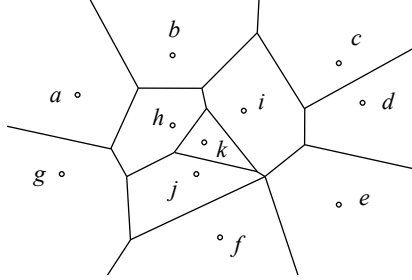
Figure 2.2: Voronoi diagram of a random set of points.

We obtain $\sigma_{\alpha\beta}(\mathbf{r}_i) = S_{\alpha\beta}(\mathbf{r}_i)/A(\mathbf{r}_i)$ where $A(\mathbf{r}_i)$ is the area of Voronoi cell corresponding to the i-th particle. We, then, interpolate the discrete stress field $\sigma_{\alpha\beta}(\mathbf{r}_i)$ onto a *fine* [1] grid of size $\sqrt{N_g} \times \sqrt{N_g}$. The discrete pressure field is defined as $p(\mathbf{r}_i) = \frac{1}{2}[\sigma_{xx}(\mathbf{r}_i) + \sigma_{yy}(\mathbf{r}_i)]$. The spatial average of $p(\mathbf{r}_i)$ is $\langle p \rangle = N_g^{-1} \sum_i p(\mathbf{r}_i)$ and the fluctuating part of $p(\mathbf{r}_i)$ is denoted by $\delta p(\mathbf{r}_i) = p(\mathbf{r}_i) - \langle p \rangle$. Table 2.1 lists the average pressure values at various ϕ. While the average shear stress vanishes, the local values $\sigma_{xy}(\mathbf{r}_i)$ are non zero. The mean squared averages are expressed as $\langle \delta p^2 \rangle = N_g^{-1} \sum_i \delta p^2(\mathbf{r}_i)$ and $\langle \sigma_{xy}^2 \rangle = N_g^{-1} \sum_i \sigma_{xy}^2(\mathbf{r}_i)$. In Fig. 2.3, $\langle \delta p^2 \rangle$ and $\langle \sigma_{xy}^2 \rangle$ are plotted against $\langle p \rangle$. The relative fluctuations, with respect to $\langle p \rangle$, are also shown in the inset. Note that (relative) fluctuations become stronger as $\langle p \rangle$ is decreased toward jamming transition and then they saturate when $\langle p \rangle$ approaches zero. This is in agreement with the systems with a lower ϕ being more heterogeneous.

$p(\mathbf{r}_i)$ and $\sigma_{xy}(\mathbf{r}_i)$ are shown in Fig. 2.4 . $p(\mathbf{r}_i)$ looks more anisotropic and heterogeneous at $\phi = 0.85$ than it does at $\phi = 0.925$. $\sigma_{xy}(\mathbf{r}_i)$, however, does not seem as sensitive to ϕ; both packing fractions contain maximum shear planes along the diagonals. We will discuss the observed heterogeneities and

---

[1]The grid spacing is $d_B/3$ and we ensure that Voronoi cells contain at least one grid point.

Table 2.1: Measured average pressure $\langle p \rangle$ at various packing fractions ϕ.

ϕ	$\langle p \rangle$
0.85	2.1×10^{-3}
0.855	3.6×10^{-3}
0.86	5.1×10^{-3}
0.865	6.7×10^{-3}
0.87	8.4×10^{-3}
0.875	1.0×10^{-2}
0.88	1.2×10^{-2}
0.89	1.6×10^{-2}
0.9	1.9×10^{-2}
0.925	2.9×10^{-2}
0.95	4.0×10^{-2}
0.975	5.1×10^{-2}
1.0	6.3×10^{-2}

anisotropy of the stress structure in the following sections.
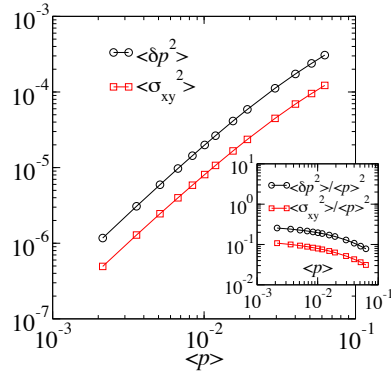
Figure 2.3: Mean square of the fluctuating local pressure $\langle \delta p^2 \rangle$ and shear stress $\langle \sigma_{xy}^2 \rangle$ versus $\langle p \rangle$. The inset is the same as the main plot but scaled by $\langle p \rangle^2$.

13

(a) $p(\mathbf{r}_i)$ for $\phi = 0.85$ (b) $p(\mathbf{r}_i)$ for $\phi = 0.925$

(c) $\sigma_{xy}(\mathbf{r}_i)$ for $\phi = 0.85$ (d) $\sigma_{xy(\mathbf{r}_i)}$ for $\phi = 0.925$
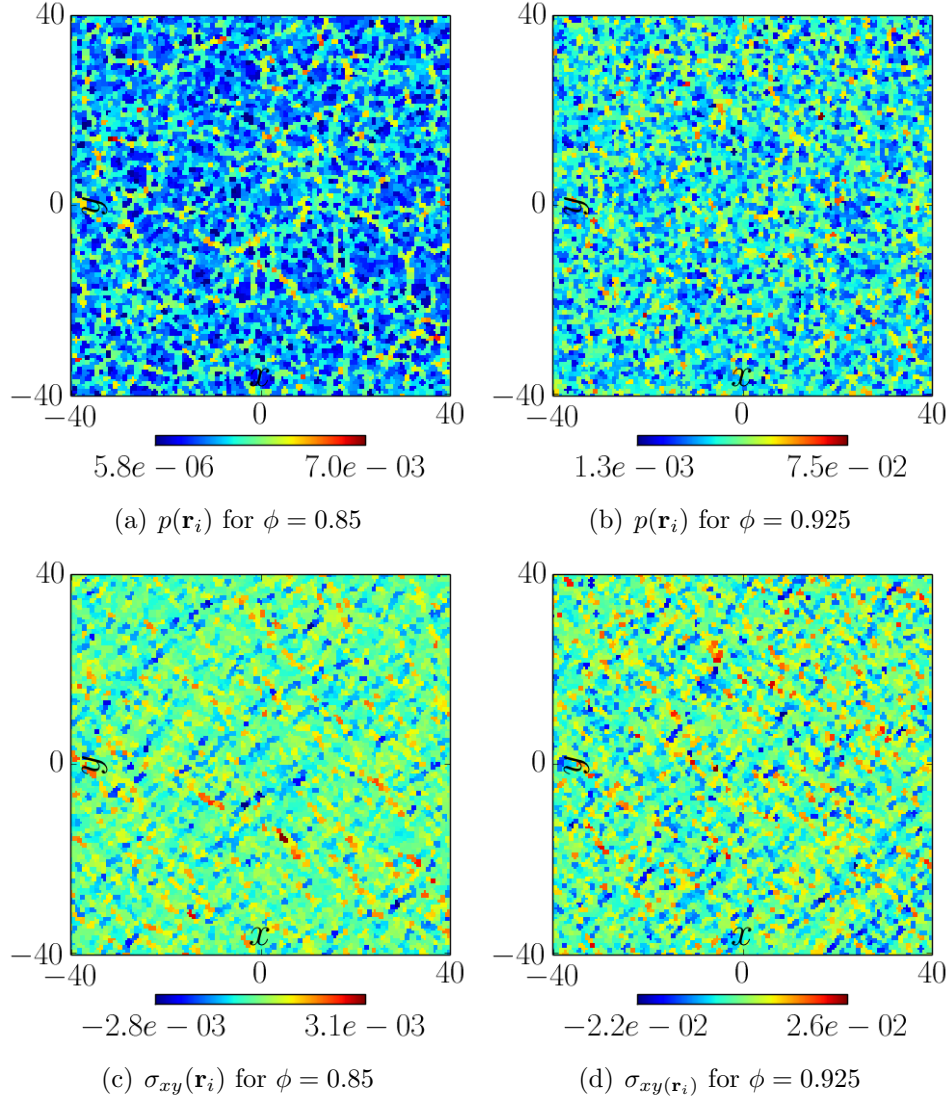
Figure 2.4: Snapshots of the real space local pressure and shear stress fields.

14

2.4 Stress Correlations

The most complete previous study on the structure of stress correlations in particle packings is the work by Henkes and Chakraborty (HC) [15]. They studied a field theory in two dimensions based on the Airy stress function and wrote down, to lowest non-trivial order, the most generic action consistent with the symmetries of globally isotropic loading. Any stress field derived from the Airy stress function automatically satisfies force balance, so force balance is enforced in their theory by construction. In their theory, to lowest order in q, the second order correlations in p had the form: $s_p(q) \sim [1 + (\xi q)^2]^{-1}$ where ξ had dimension of length. Correlations in σ_{xy} were found to be anisotropic and scaled as $s_p(q) \sim q^{-4} q_x^2 q_y^2 [1 + (\xi q)^2]^{-1}$.

Our data for pressure and shear stress correlations are not inconsistent with theirs over the range of lengths they studied ($L \approx 30$). However, surprisingly, we observe a departure from HC prediction that occurs at a wavelength longer than the longest wavelength reported by them. Additionally, they found that local correlations in the shear stress had an r^{-2} decay in real space. We suspect this to be closely related to the r^{-2} decay we observe in the modified pressure correlation functions (discussed below). The pressure correlations in real space (also discussed below), in contrast, dont agree with their proposed form of $r^{-1/2} e^{-r^2}$. We suspect this is due to the excess power we find at long wavelength

In this section, we examine the stress correlations in both Fourier space and real space and study its sensitivity to the jamming transition.

2.4.1 Correlations In Fourier Space

To obtain the data, we take the two-dimensional discrete Fourier transform of $\delta p(\mathbf{r}_i)$ and $\sigma_{xy}(\mathbf{r}_i)$. We discuss the pressure fluctuations first. In Fourier space, we obtain

$$\delta p(\mathbf{q}) = \sum_j \delta p(\mathbf{r}_j) \, e^{-i\mathbf{q} \cdot \mathbf{r}_j}, \qquad (2.1)$$

with $\mathbf{q} = 2\pi L^{-1}(n\hat{\mathbf{x}} + m\hat{\mathbf{y}})$ where m and n are integers and $\hat{\mathbf{x}}$ and $\hat{\mathbf{y}}$ are unit vectors along the x and y axes. We then calculate the two dimensional structure factor $s_p(\mathbf{q})$ on a two dimensional grid

$$s_p(\mathbf{q}) = \frac{1}{N_g} \frac{|\delta p(\mathbf{q})|^2}{\langle \delta p^2 \rangle}, \qquad (2.2)$$

where $s_p(\mathbf{q})$ is defined as the power spectrum of local pressure field normalized by its mean square fluctuations.

We, now, will consider the isotropic contributions of $s_p(\mathbf{q})$. The results were averaged over evenly spaced intervals in $\log(q)$ where $q = 2\pi L^{-1}(m^2 + n^2)^{1/2}$ is the wave number. Note that this process automatically averages over angles, so it produces only the isotropic contribution $s_p(q)$. With $L = 320$ particle diameters, we can investigate the range of $(2\pi)^{-1}q$ from L^{-1} to $(\sqrt{2}L)^{-1}\sqrt{N_g}^2$. The angle-averaged correlations $s_p(q)$ measured for different packing fractions ϕ is shown in Fig. 2.5. The sudden drop, about one order of magnitude, at high q values and flat spectrum at intermediate q, which extends further out to low-q values, are in agreement with HC theory. But, the curves start to go up very rapidly (about one order of magnitude) at a

---

$^2 n$ (or m) ranges from $-\sqrt{N_g}/2$ to $\sqrt{N_g}/2$.
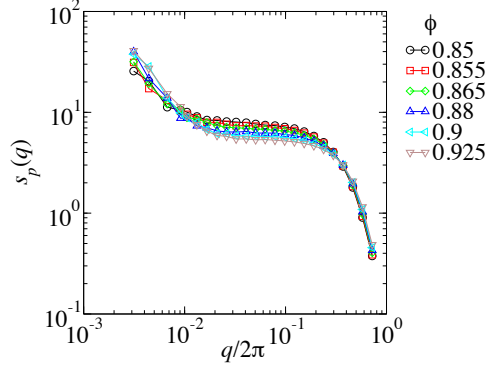
Figure 2.5: Scaling of the isotropic pressure correlation function $s_p(q)$ for various ϕ.

rather long wavelength that is not predicted in their theory. We suspect that HC were not able to detect this feature in their numerical simulations due to small system size. Furthermore, we note that this length-scale is in rough agreement for the characteristic length-scale observed in the elastic response of structural glasses reported by Tanguy and co-workers [23, 21, 22, 48]. The flat region in loose packings extend to a lower q than it does in denser systems which implies a grown length in real space. However, it is difficult to quantify this phi-dependent crossover by simply examining the power spectrum. We will discuss a related, alternative, point of view below when we study the variance of the coarse-grained pressure field.

Similarly, the shear structure factor in Fourier space is presented as

$$s_{xy}(\mathbf{q}) = \frac{1}{N_g} \frac{|\sigma_{xy}(\mathbf{q})|^2}{\langle \sigma_{xy}^2 \rangle}, \tag{2.3}$$

where $\sigma_{xy}(\mathbf{q}) = \sum_j \sigma_{xy}(\mathbf{r}_j)\, e^{-i\mathbf{q}\cdot\mathbf{r}_j}$. Figure 2.6 shows the angular structure of the shear correlations for $\phi = 0.85$ and $\phi = 0.925$. We remind the readers

17

(a) $s_{xy}(\mathbf{q})$ at $\phi = 0.85$ (b) $s_{xy}(\mathbf{q})$ at $\phi = 0.925$
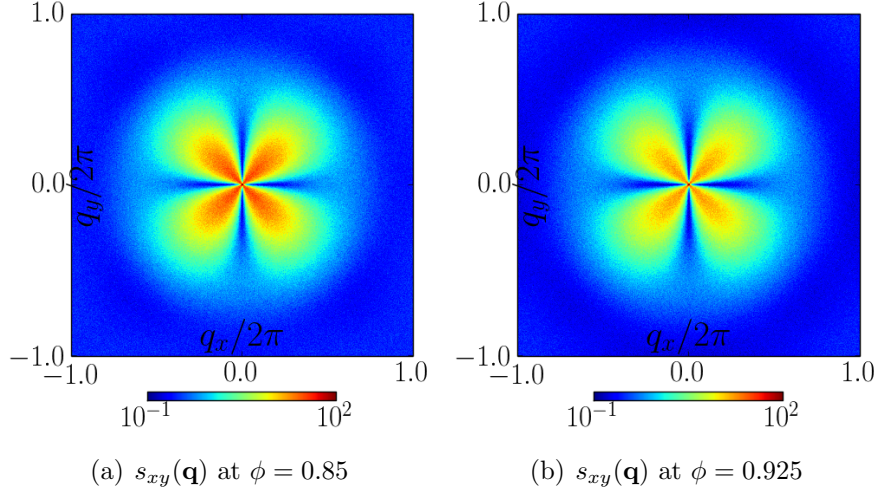
Figure 2.6: Maps of $s_{xy}(\mathbf{q})$ using a decimal log scale.

that maximum local shear planes are along the diagonals where the shear correlations are strong [see the real space picture in Fig. 2.4(c) and (d)]. It should be noted that the statistical average shows a $\cos(4\theta)$ symmetry. The shear stress power spectrum also shows the same deviations and excess power at low q as did the pressure power spectrum.

2.4.2   Real Space Correlation Functions

HC predicted the real-space pressure correlation functions from the form of their Fourier-space correlation functions which had the form $r^{-1/2}e^{-r^2}$. They concluded that local pressure has short range correlations which fall off beyond a scale set by ξ. Our data, however, does not show a simple scaling behavior, particularly at longer wavelengths, which prevents us from doing a similar analytical calculation. Instead, we compute the real space correlations by performing an inverse discrete Fourier transform on the two
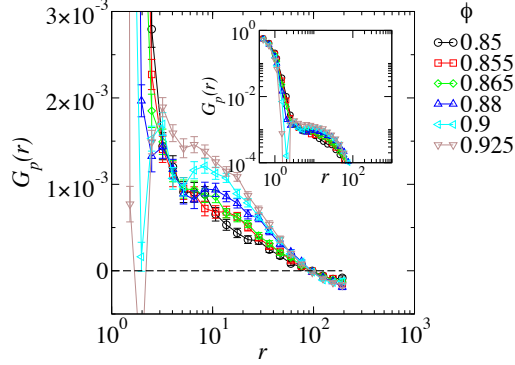
Figure 2.7: Scaling of the real space isotropic pressure correlation function $G_p(r)$ for various ϕ on lin-log scale. The inset plots $G_p(r)$ on a logarithmic logarithmic scale.

dimensional q grid

$$
\begin{aligned}
G_p(\mathbf{r}_j) &= \frac{\langle \delta p(\mathbf{r}_j) \delta p(0) \rangle}{\langle \delta p^2 \rangle} \\
&= \frac{1}{N_g} \sum_{\mathbf{q}} s_p(\mathbf{q}) \, e^{i\mathbf{q} \cdot \mathbf{r}_j}.
\end{aligned} \tag{2.4}
$$

We, now, consider isotropic contributions of $G_p(\mathbf{r}_i)$. The results were averaged over evenly spaced intervals in $\log(r)$ where r is the distance that ranges from 0 to $L/\sqrt{2}$. The angle-averaged correlations $G_p(r)$ measured for different ϕ is shown in Fig. 2.7. The shapes of these curves are not so simple to interpret and differ dramatically with varying ϕ. It looks that the pressure fluctuations have short range correlations that fall off by about two orders of magnitude beyond about two particle diameter (see the inset). But then they form a shoulder and decay slower past this point and finally cross through zero at $r \approx 100$.

Real space correlations in the local shear stress are, however, anisotropic

19
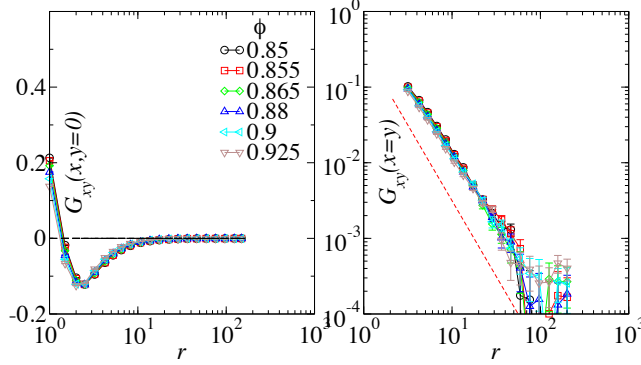
Figure 2.8: Scaling of the real space shear stress correlation $G_{xy}(\mathbf{r})$ at $\theta = 0$ (left) and $\theta = \pi/4$ (right) for various ϕ. The dashed line on the right panel illustrates r^{-2} decay.

and admit long range power law correlations r^{-2} along the diagonal regardless of ϕ(see Fig. 2.8 right). Along the axes, however, we see negative correlations as shown in Fig. 2.8 left. We present our modified version of correlation functions in the next section which has a similar angular and r dependence.

2.4.3 Modified Correlation Functions

We focus on a *modified* real-space correlations that determines correlations along *locally determined* principal stress directions (see Appendix A.1). This function $G^{\mathrm{mod}}(r)$ gives a quantitative measurement of the average effect of force chains of length r in the packing. A positive value at distance r indicates that the two particles are connected by a chain of contacting particles and the force is being transmitted through the chain from one particle to the other. Negative values of the correlation correspond to situations where two particles at distance r tend to be aligned along their minor stress axes.

The calculated correlation functions $G_n^{\mathrm{mod}}(r)$ along major stress direction
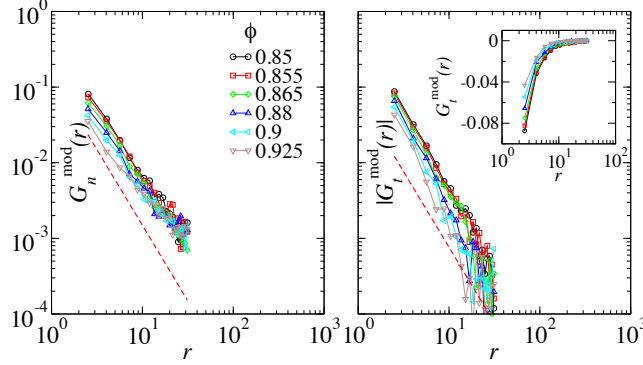
Figure 2.9: Spatial pressure correlations $G_n^{\mathrm{mod}}(r)$ along the major stress direction **n** (left) and $G_t^{\mathrm{mod}}(r)$ along the minor stress direction **t** for various ϕ. Note that the sign of $G_t^{\mathrm{mod}}(r)$ is exclusively negative. The inset shows the correlation function on a linear logarithmic scale. The line illustrates the power law decay of r^{-2}.

n and $G_t^{\mathrm{mod}}(r)$ along minor stress axis **t** are plotted in Fig. 2.9 for various ϕ. The anisotropic version of the correlation function shows a clear power law behavior r^{-2} up to $r \approx 20$ regardless of the distance from the jamming transition and with positive $G_n^{\mathrm{mod}}(r)$ and negative $G_t^{\mathrm{mod}}(r)$. We suspect this to be closely related to HC's results on the shear stress correlations; they found that local correlations in the *shear* stress had an r^{-2} decay in real space. Moreover, they showed that the real-space shear correlation function had an angular dependence with negative and positive correlations. We do not go out any further in r because at $r \approx 20$, the signal strength is below the noise floor for the amount of statistics we were able to obtain.

We have measured the stress correlations both in real and Fourier space and found them to have surprisingly little dependence on the distance to the jamming. Our next stress analysis is rather different and deserve some discussion here. If one has access to the power spectrum of the pressure field,

one may compute the strength of the fluctuations in the coarse-grained field by simple application of the convolution theorem. By varying the coarse-graining size, one would have a better insight about the scaling of these fluctuations with size.

2.5 Coarse-grained Stress

In this section we study the statistical properties of the stress field as a function of coarse-graining size. We will demonstrate a characteristic change in the nature of the fluctuations at large coarse-graining size and find the crossover in the statistics to depend on the distance to jamming.

We also study the average magnitude of the coarse-grained deviatoric shear stress. Even in an isotropically prepared sample with a globally hydrostatic stress state, the deviatoric magnitude is large at small scales. This local anisotropy appears due to strongly correlated forces along the direction of chains and vanishes globally when stress reaches its hydrostatic state. This observations allows us to identify an important length quantifying the size of force networks. The observation of the kink in both the pressure fluctuations and the deviatoric magnitude signify to us that this length scale is a rather robust feature.

2.5.1 Fluctuations In Coarse-grained Pressure

Let us denote the coarse-grained stress field as $\Sigma_{\alpha\beta}(\mathbf{r}_i, R)$ where R is the coarse-graining scale. We assume that our coarse-graining procedure is such that the spatial average of the coarse-grained field do not depend on R and remains unchanged. The coarse-grained pressure field $P(\mathbf{r}_i, R)$ is defined as half the trace of $\Sigma_{\alpha\beta}(\mathbf{r}_i, R)$ with the fluctuating part denoted by $\delta P(\mathbf{r}_i, R)$. We assume that our coarse-graining procedure is such that the spatial average of the coarse-grained field do not depend on R and remains unchanged. This leads to $N_g^{-1} \sum_i P(\mathbf{r}_i, R) = \langle p \rangle$. The strength of fluctuations at various R is

(a) $R = 2.0$ (b) $R = 4.0$
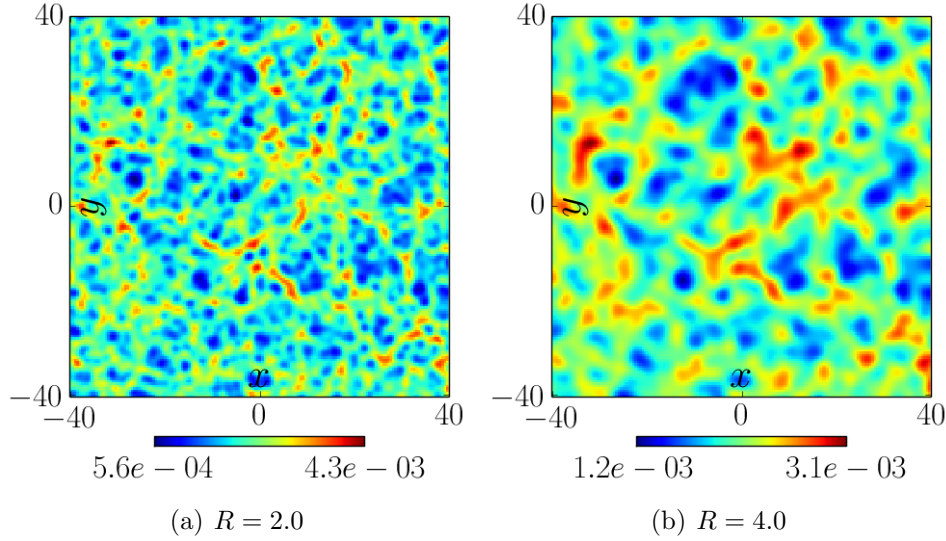
Figure 2.10: Snapshots of real space coarse-grained pressure field $P(\mathbf{r}_i, R)$ at $\phi = 0.85$.

quantified by $\langle \delta P^2 \rangle_R = N_g^{-1} \sum_i \delta P^2(\mathbf{r}_i, R)$.

Figure 2.10 shows $P(\mathbf{r}_i, R)$ for various R at $\phi = 0.85$. It is clear that the inhomogeneities associated with the coarse-grained pressures are more pronounced at small R values. As R is increased, $P(\mathbf{r}_i, R)$ become more uniform and isotropic in space. Chain-like structures are apparent at finest R but they start to disappear at larger R.

In Fig. 2.11 left, we plot $R^2 \langle \delta P^2 \rangle / \langle p \rangle^2$ versus R for various ϕ. In the insets, we present $\langle \delta P^2 \rangle / \langle p \rangle^2$ versus R. The scaled fluctuations $R^2 \langle \delta P^2 \rangle / \langle p \rangle^2$ increase monotonically as ϕ ranges from 0.925 to 0.85 at any particular coarse-graining length-scale. The primary trend in the data is to follow approximately the R^{-2} scaling at small R expected from counting statistics, however, the dramatic *departures* from R^{-2} at large R show a pronounced ϕ dependence. For all ϕ, there is a relatively sharp crossover from a small
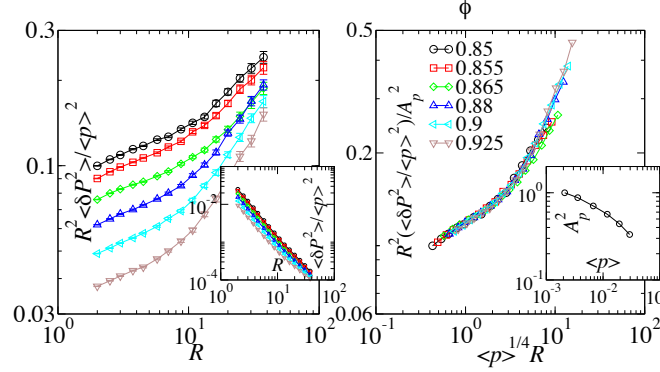
Figure 2.11: $R^2\langle \delta P^2\rangle/\langle p\rangle^2$ versus R (left) and $R^2\langle \delta P^2\rangle/\langle p\rangle^2$ scaled by A_p^2 versus $\langle p\rangle^{1/4}R$ (right) at various ϕ. The insets show $\langle \delta P^2\rangle/\langle p\rangle^2$ versus R (left) and the scale parameter A_p^2 versus $\langle p\rangle$ (right).

R regime to a large R regime where $\langle \delta P^2\rangle/\langle p\rangle^2$ decay much more slowly than the counting argument would indicate. We denote the length at which the crossover occurs by ξ_p. This length in rough agreement with the visual impression of the chains observed in Fig. 2.1, with the systems closer to jamming crossing over at larger ξ_p.

In Fig. 2.11 right, we show that the data can be made to collapse for various ϕ when plotting $R^2(\langle \delta P^2\rangle/\langle p\rangle^2)/A_p^2$ versus $\langle p\rangle^{1/4}R$. Here A_p^2 is a scale parameter which is chosen by hand to obtain a good collapse. In the insets, we plot A_p^2 which is normalized to its value at $\phi = 0.85$. The $\xi_p \sim \langle p\rangle^{-1/4}$ scaling is consistent with a divergence at ϕ_c.

2.5.2 Anisotropy In Coarse-grained Stress

The deviatoric magnitude of the coarse-grained stress field $\Sigma_{\alpha\beta}(\mathbf{r}_i, R)$ is defined as

$$\tau^2(\mathbf{r}_i, R) = \frac{1}{4}(\Sigma_{xx} - \Sigma_{yy})^2 + \Sigma_{xy}^2. \tag{2.5}$$

25
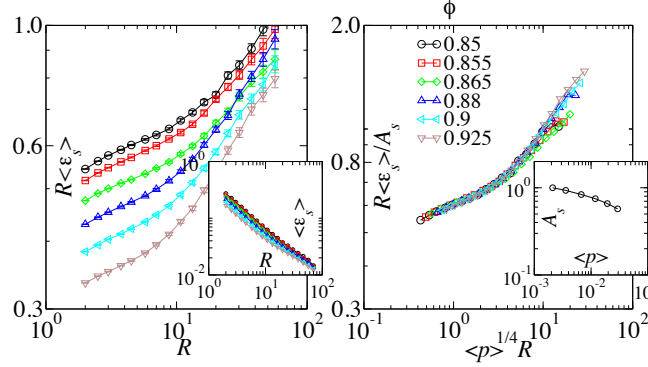
Figure 2.12: $R\langle\varepsilon_s\rangle$ versus R (left) and $R\langle\varepsilon_s\rangle$ scaled by A_s versus $\langle p\rangle^{1/4}R$ at various ϕ. The insets show $\langle\varepsilon_s\rangle$ versus R (left) and the scale parameter A_s versus $\langle p\rangle$ (right).

Intuitively, if a given region contains a single dominant force chain, the direction of the eigenvector of $\Sigma_{\alpha\beta}(\mathbf{r}_i, R)$ with larger eigenvalue should point along it, while a region containing multiple force chains oriented along various directions or no force chain at all should have a hydrostatic stress with $\tau(\mathbf{r}_i, R) \approx 0$. We let $\varepsilon_s(\mathbf{r}_i, R) \doteq \tau(\mathbf{r}_i, R)/\langle p\rangle$ characterize the degree of anisotropy in the coarse-grained tensor stress tensor and denote its spatial average by $\langle\varepsilon_s\rangle$.

In Fig. 2.12 left, we plot $R\langle\varepsilon_s\rangle$ versus R for various ϕ. There is no qualitative shape difference visible between these curves and $R^2\langle\delta P^2\rangle/\langle p\rangle^2$ already discussed in the previous section. Additionally, in Fig. 2.12 right, we show that the data can be also made to collapse for $R\langle\varepsilon_s\rangle$ versus $\langle p\rangle^{1/4}R$ with the scale parameter A_s. The crossover length ξ_s scales as $\langle p\rangle^{-1/4}$, similar to ξ_p, and quantifies the average extent of force chains in the system. This length approaches the size of the system at the transition and diverges in the thermodynamic limit.
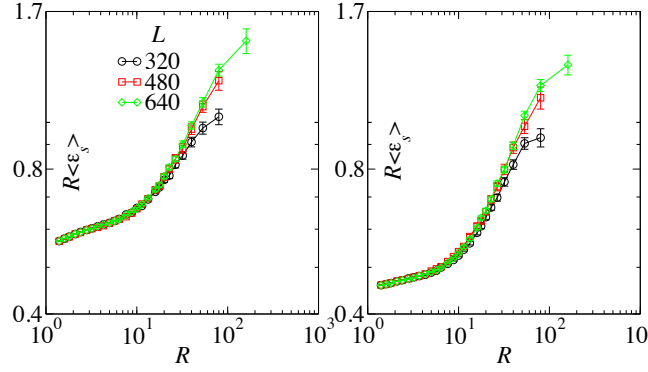
Figure 2.13: Illustration of the system size effect in $R\langle\varepsilon_s\rangle$ versus R for $L = 320, 480,$ and 640 at $\phi = 0.85$ (left) and $\phi = 0.88$ (right).

It should be noted that we obtain similar values for the scale parameters in systems which are larger than the $L = 320$ one shown here emphasizing that system size plays no role in the crossover behavior for the range of ϕ studied (see Fig. 2.13). However, at $\phi = 0.85$, our estimates for ξ_s do become sensitive to L for $L < 320$. This dictates our rather large choice for L.

2.6 Discussion And Summary

In this chapter, we have used several numerical methods to analyze stress correlations of particle packings in view of extracting a characteristic size. We have shown that there are characteristic lengths in the stress field that diverge in similar ways as the confining pressure approaches zero from above the transition point. In a first step, the power spectrum of the local pressure and shear stress agree with a field-theoretic framework proposed by HC at short to intermediate wavelengths (where the power is flat in Fourier space), but contain significant excess power at wavelengths larger than about 50 to 100 particle diameters, with the specific crossover point going to larger wave length at decreasing pressure, consistent with a divergence at $p = 0$. We suspect that these stress correlations were missed in previous studies by other groups due to limited system size [49].

Then, a modified version of the correlation function was defined to account for the inherent anisotropy in internal stresses. This approach was able to detect a different type of correlations which ranged over a long distance and decays as r^{-2}. The observed behavior was in close agreement with the power law decay of shear stress correlations in real space proposed by HC.

Next, spatial fluctuations in coarse-grained stress were extracted at different coarse-graining levels and found to decay slower than expected from theory for uncorrelated samples. We have also examined anisotropy in the coarse-grained stress, ε_s. When forces were replaced by randomly distributed forces, ε_s of these data decayed in close agreement with the expectations from the central limit theorem, whereas anisotropy in the *real* data showed

a strikingly different trend. We found a clear transition, marked by a special coarse-graining size, from the expected uncorrelated behavior to a fully correlated one which was a signature of the stress structure. Both measurements exhibited clear characteristic length-scales ξ_s and ξ_p which scaled as $\langle p \rangle^{-1/4}$ and ,therefore, were consistent with a divergence at ϕ_c. To our knowledge, in isotropically compressed samples, no metric measurement of *force chains* had led to correlation lengths longer than a few particle diameters – largely independent of the distance to the jamming transition.

Chapter 3

Elastic Response

3.1 Introduction

For many years now, it has been known that packings of elastically deformable particles, confined by a compressive external hydrostatic pressure, exhibit an anomalous elastic response near the limit of zero confining pressure, p [10, 11]. Mason and Weitz first observed this experimentally in sheared emulsions where the low frequency linear elastic storage modulus showed a sharp transition by many orders of magnitude as the volume fraction of the particles, ϕ, crossed the nominal random-close-packing volume fraction, ϕ_c [35]. This result generated many theoretical, numerical, and experimental studies over the next decade (for a review, see reference [51]).

A seminal numerical study by O'Hern et al. [40] showed that in a simple, frictionless disc/sphere packing model, the shear modulus vanished algebraically as ϕ went to its critical value, ϕ_c, while the compression modulus remained finite. Several later works related this anomalous vanishing of the shear modulus to an excess of low energy, "floppy", eigenmodes below an energy scale, ω_*^2, that vanished as $\phi \to \phi_c$ [52, 53]. However, the relationship between the energy scale at which these excess modes appear and various lengthscales associated with them has remained more subtle.

Much of the early work connecting the vanishing of ω_* to the emergence of diverging characteristic lengths neglected the role of quenched stresses in the contact network [13, 44, 9]. Within this stress-free context, it was generally agreed upon that there was one length scale associated with rigidity, l_* [13], and another length associated with the structure of the eigenmodes at the ω_*^2 energy scale, l_T. In particular, Xu et al. [54] showed that there was a change

in eigenmode character at the anomaly in the density of states. Silbert et al. [46] did include the effects of quenched stresses and attempted to spatially decompose these low energy modes at a given energy level – in the low anomalous regime or in the higher energy Debye regime – into longitudinal and transverse waves. They were able to show that the transverse power at the transition frequency, ω_*, peaked at a wave-vector with a length-scale, ξ_T that grew roughly as $\delta\phi^{-1/4}$. They argued that an analogous measurement for the longitudinal power would show a ξ_L that would scale in the same way with $\delta\phi$ as ω_*^{-1} but were unable to demonstrate this numerically.

More recently, Lerner and co-workers [7] have shown, in a repulsive soft-disc system that the elastic response to a point perturbation is governed by l_T. This result seemingly contradicted earlier work by Ellenrboek and co-workers [9] who showed that the point response (also in models including the effect of the quenched forces) is controlled by l_* rather than l_T. One of the central results of the present work reconciles these two viewpoints. We show that the longitudinal contribution to the point response is much more sensitive to pressure with an associated length $\xi_L \sim p^{-0.4}$ (close to the $l_* \sim p^{-1/2}$ result), and the transverse contribution is much less sensitive to pressure with $\xi_T \sim p^{-1/4}$ (completely analogous to l_T scaling). However, the overall point response is predominantly transverse at jamming (the ratio of shear to compression modulus goes to zero at jamming), so in analyses that do not carefully separate longitudinal from transverse, the dominant effect will come from ξ_T and one would observe a length growing like $p^{-1/4}$.

We also probe the local elastic modulus by imposing homogeneous shear using no slip boundary conditions with boxes of various size, R. The rigid

constraints imposed at the walls squelch non-affine relaxations and raise the value of shear modulus beyond its fully relaxed value. We find that the constrained shear modulus recedes to its limit as $\mu(R)/\mu_\infty - 1 \sim p^{-1/2}R^{-1}$. This is consistent with l_* governing the shear modulus in finite regions driven with no-slip boundary conditions. Physically this means that the size of the sample one needs to obtain a well-converged measure of the true relaxed shear modulus diverges at jamming.

Finally, we study the unconstrained response to global, homogeneous strain (both volumetric and shear). The power spectrum of the response is roughly consistent with previous reports on Lennard-Jones [33, 23] where one observed $u^2(q) \sim q^{-2}$ but with important details not observed before and some interesting sensitivity to jamming. In particular we show that, under imposed shear, both transverse and longitudinal power have an anisotropic form resulting from a few strong displacement quadrupoles. Under imposed dilation/compression, the transverse and isotropic power are anisotropic on average, but, like the shear response, are dominated by a few strong localized displacement quadrupoles. As $p \to 0$, very surprisingly, the transverse power spectrum remains largely unchanged. The longitudinal power spectrum, on the other hand, for both applied shear and applied dilation, shows a pronounced p sensitivity. It develops a characteristic feature at short wavelength that intensifies as $p \to 0$. The coherent shear zones, still visible in the transverse field near $p = 0$, become essentially incoherent zones of local dilation/expansion in the longitudinal piece with a characteristic size of roughly 5 particle diameters with no coherent organization of the dilatancy field as at higher p.

The rest of this chapter is organized as follows. In Section 3.2, we discuss the point response. Section 3.3 discusses the response to homogeneous deformation with no slip boundary conditions, and recalls how one computes the elastic moduli using linear response theory. In Section 3.4, we describe the response to homogeneous deformation of the full system with periodic boundary conditions.

3.2   Point Response

We start here by studying the general aspects of linear point response (Green's function) in amorphous systems. Our primary assumption here is that, macroscopically, these systems have well defined average isotropic elastic modulus tensor, where it can be described by only two elastic moduli, the bulk modulus K and the shear modulus μ. The Fourier transform of the elastic Green's function of the system scales as q^{-2}. Since the system is disordered and heterogeneous; i) the response to a point load will not precisely follow the homogeneous continuum solution, and ii) each particular choice of particle to exert the force will result in a slightly different response function. However, on average, and at long lengths, we expect continuum homogeneous elasticity to provide a good description. The question here is how the fluctuations away from the continuum description die away at long lengths and how this depends on proximity to jamming.

It should be mentioned that the elastic Green's function in real space will depend on the system size L and exhibit a logarithmic divergence in two dimensions, i.e. $\langle \mathbf{u}.\mathbf{u} \rangle \sim \log(L)$ [5, 7]. Our data (not shown here) confirms that the real ensemble averaged Green's function quickly converges to a well defined value as the distance from the local perturbation becomes much larger than the typical particle size.

The initial configurations and their preparation are similar to those described in Section 2.3. The interaction potential of the system depends on the positions of the particles $\mathbf{r}_i$ and may be written as a function of the full set of distances r_{ij} between pairs of interacting particles $\mathcal{U} = \sum_{ij} U(r_{ij})$

where the index ij runs over all pairs of particles.

3.2.1 Harmonic Approximation

Perturbing the energy about small displacements $u_{i\alpha}$ from their original positions $r_{i\alpha}$ reads

$$\mathcal{U} \approx \mathcal{U}_0 + \mathring{F}_{i\alpha} \, u_{i\alpha} + \frac{1}{2} \, u_{i\alpha} \, H_{i\alpha j\beta} \, u_{j\beta}, \tag{3.1}$$

where $u_{i\alpha}$ is the displacement, $H_{i\alpha j\beta} = \partial^2 \mathcal{U}/\partial r_{i\alpha} \partial r_{j\beta}|_{u_{i\alpha} \to 0}$ is the Hessian and $\mathring{F}_{i\alpha} = \partial \mathcal{U}/\partial u_{i\alpha}|_{u_{i\alpha} \to 0}$. An equation of motion for the displacements is specified by the condition that the system remains at mechanical equilibrium in response to an external force $F_{i\alpha}^{\text{ext}}$, that is $\partial \mathcal{U}/\partial r_{i\alpha} = F_{i\alpha}^{\text{ext}}$. Differentiating (3.1) with respect to $r_{i\alpha}$ leads to

$$H_{i\alpha j\beta} \, u_{j\beta} = F_{i\alpha}^{\text{ext}} - \mathring{F}_{i\alpha}. \tag{3.2}$$

We solve numerically the linear response equation in Eq. (3.2) for the displacements $u_{i\alpha}$ of all particles using the sparse matrix routines in the SciPy library. This approach directly utilizes the Hessian matrix of the system to derive the elastic displacement field. For periodic systems, this solution is defined up to rigid translations–but conventionally the solution with no translational component is chosen– since the Hessian is translationally invariant. The elements of the Hessian matrix are evaluated using the analytical form for pair potentials as in [20]. Once the Hessian matrix is assembled, we check its positive definiteness.

In order to apply the point force, a particle is chosen at random and

36

its center defines the origin of the system. In order to maintain mechanical stability, a compensation force of $F_y = F/N$ is applied on all particles so that $\sum_i F_{iy}^{\text{ext}} = 0$ [22]. Here F is the magnitude of the external force and N is the total number of particles. A typical example for the field $u_{i\alpha}$ is shown in Fig. 3.1(a).

3.2.2   Continuum Solution

We have assumed that the medium is homogeneous, isotropic, and linearly elastic, so that the elastic properties of the system are fully described by the bulk modulus K and shear modulus μ. See Appendix B.3 for more details on how the exact continuum solution for a point response can be derived. Figure 3.1(b) illustrates a typical continuum solution in *real* space. In *Fourier* space, we obtain

$$
\begin{aligned}
u_L^{\text{cont}}(\mathbf{q}) &= \frac{F \sin(\theta)}{(K + \mu)q^2\, V}, \\
u_T^{\text{cont}}(\mathbf{q}) &= \frac{F \cos(\theta)}{\mu q^2\, V}.
\end{aligned}
\tag{3.3}
$$

Here, $u_L^{\text{cont}}(\mathbf{q})$ and $u_T^{\text{cont}}(\mathbf{q})$ are the longitudinal and transverse amplitudes of the displacements, F is the applied force magnitude, θ is the angle of the force vector with respect to the x axis, and V is the volume (area in two dimensions).

(a) Actual point response   (b) Continuum estimate
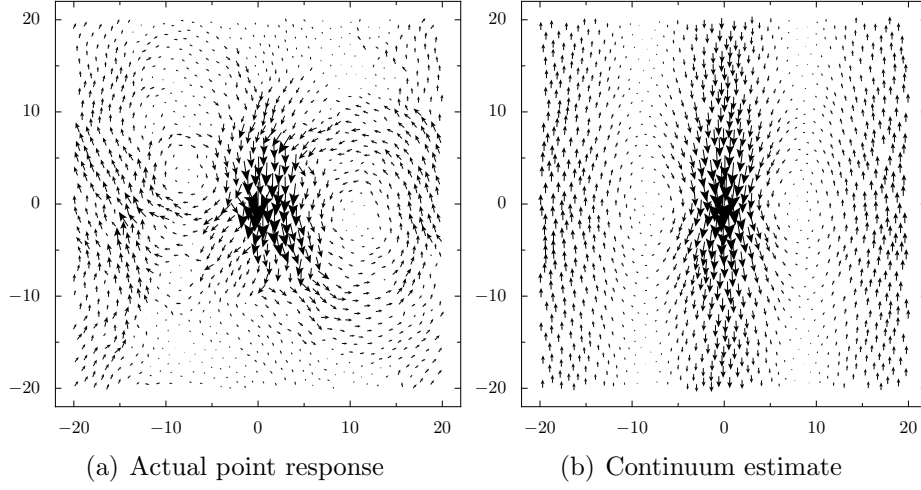
Figure 3.1: Arrows represent the displacements in response to a point force.

3.2.3 Displacement Field Decomposition

We present the *actual* point response by its Fourier longitudinal and transverse amplitudes, $u_L(\mathbf{q})$ and $u_T(\mathbf{q})$, where $\mathbf{q}$ is the wave vector. To obtain the data, we interpolate the discrete displacements $u_{i\alpha}$ on a regular *fine* grid of size $\sqrt{N_g} \times \sqrt{N_g}$ and then take the two-dimensional discrete Fourier transform of the interpolated field $u_\alpha(\mathbf{r}_j)$

$$
\begin{aligned}
u_L(\mathbf{q}) &= \sum_j u_\alpha(\mathbf{r}_j) n_\alpha \, e^{i\mathbf{q}\cdot\mathbf{r}_j}, \\
u_T(\mathbf{q}) &= \sum_j u_\alpha(\mathbf{r}_j) n_\alpha^\perp \, e^{i\mathbf{q}\cdot\mathbf{r}_j}.
\end{aligned}
\tag{3.4}
$$

Here $n_\alpha = q_\alpha/q$ is the unit vector along $\mathbf{q}$ and $u_L(\mathbf{q})$ and $u_T(\mathbf{q})$ denote the longitudinal and transverse displacement amplitude.

We then calculate the two-dimensional structure factors $s_L(\mathbf{q})$ and $s_T(\mathbf{q})$

on the two-dimensional q space averaged over position and members in the ensemble

$$
\begin{aligned}
s_L(\mathbf{q}) &= \frac{1}{N_g} \frac{|u_L(\mathbf{q})|^2}{\langle \mathbf{u}.\mathbf{u} \rangle}, \\
s_T(\mathbf{q}) &= \frac{1}{N_g} \frac{|u_T(\mathbf{q})|^2}{\langle \mathbf{u}.\mathbf{u} \rangle},
\end{aligned}
\tag{3.5}
$$

where $\langle \mathbf{u}.\mathbf{u} \rangle = N_g^{-1} \sum_i \mathbf{u}(\mathbf{r}_i).\mathbf{u}(\mathbf{r}_i)$ is the mean squared displacements [1]. It must be noted that we average over square amplitudes and this means that the phase information is not contained in $s_L(\mathbf{q})$ and $s_T(\mathbf{q})$. Hence, the average Green's function cannot be reconstructed from $s_L(\mathbf{q})$ and $s_T(\mathbf{q})$.

Figure 3.2 displays the ensemble averaged structure factors $s_L(\mathbf{q})$ and $s_T(\mathbf{q})$ (rescaled by q^{-4}) for $\phi = 0.85$ and $\phi = 0.925$. The structure factors $s_L(\mathbf{q})$ and $s_T(\mathbf{q})$ rescaled by q^{-4} measured along $\theta = 0$ and $\theta = \pi/2$ are shown in Figs. 3.3 and 3.4 for $\phi = 0.85$ (left) and $\phi = 0.925$ (right). The averages were calculated by binning according to $\log q$ along q_x and q_y on the two-dimensional q grid. The dashed lines in the plots represent the continuum predictions $q^4 s_L^{\text{cont}}(\mathbf{q})$ and $q^4 s_T^{\text{cont}}(\mathbf{q})$ which can be derived from Eq. (3.3) [2].

There are several important observations to make about these plots. First, note that $u_L^{\text{cont}}(\mathbf{q})$ is precisely zero at $\theta = 0$, as the applied force contains zero longitudinal power along that direction $-f_L(q_x, q_y = 0) = 0$. This is also true for $u_T^{\text{cont}}(\mathbf{q})$ at $\theta = \pi/2$. Surprisingly, longitudinal power along $\theta = 0$ and transverse power along $\theta = \pi/2$ are present (circles in Fig. 3.3 and

---

[1]Using the Parseval's theorem, we obtain $\langle \mathbf{u}.\mathbf{u} \rangle = N_g^{-2} \sum_{\mathbf{q}} |u_L(\mathbf{q})|^2 + |u_T(\mathbf{q})|^2$.

[2]Note that $\langle \mathbf{u}^{\text{cont}}.\mathbf{u}^{\text{cont}} \rangle \to \infty$ in two dimensions and thus is evaluated on a regular grid of size $\sqrt{N_g} \times \sqrt{N_g}$.

(a) $q^4 s_L(\mathbf{q})$ at $\phi = 0.85$

(b) $q^4 s_L(\mathbf{q})$ at $\phi = 0.925$

(c) $q^4 s_T(\mathbf{q})$ at $\phi = 0.85$

(d) $q^4 s_T(\mathbf{q})$ at $\phi = 0.925$
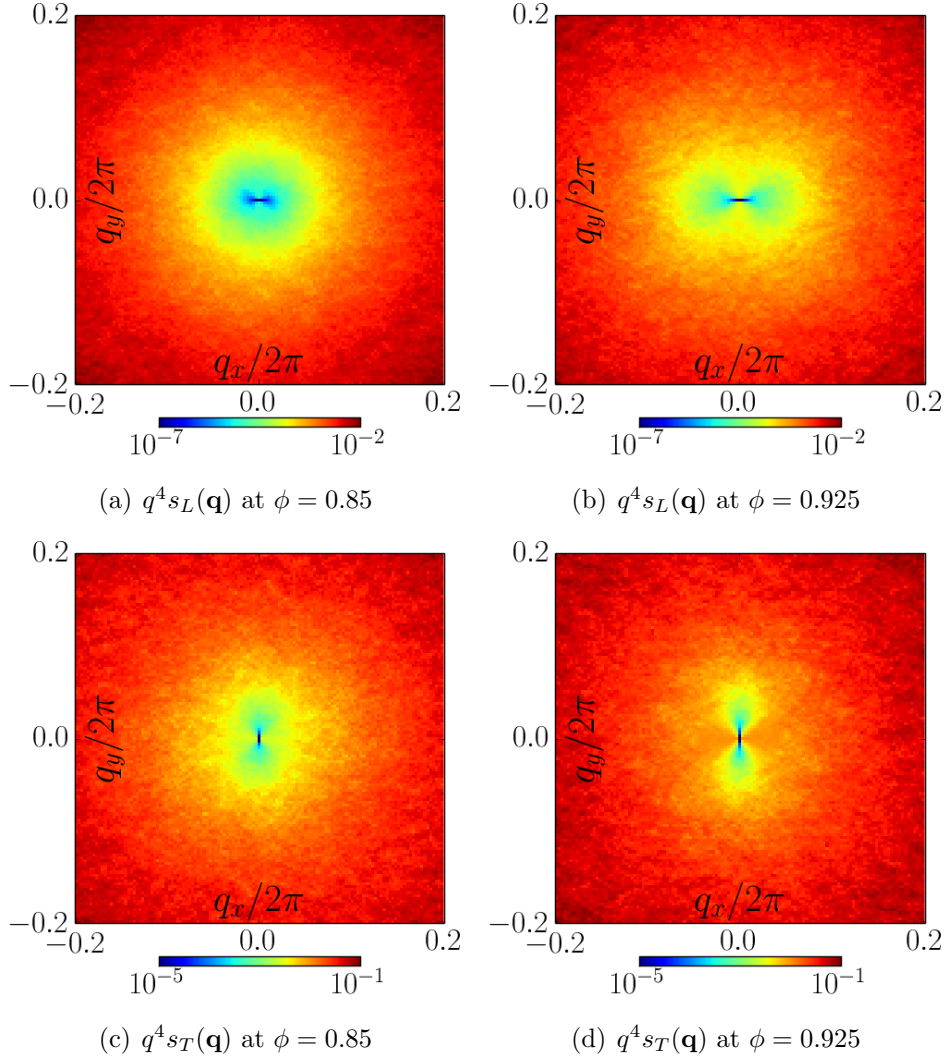
Figure 3.2: Maps of $q^4 s_L(\mathbf{q})$ and $q^4 s_T(\mathbf{q})$ using a decimal log scale plotted for $\phi = 0.85$ and $\phi = 0.925$. Note that the power must be invariant under $\theta \to -\theta$.
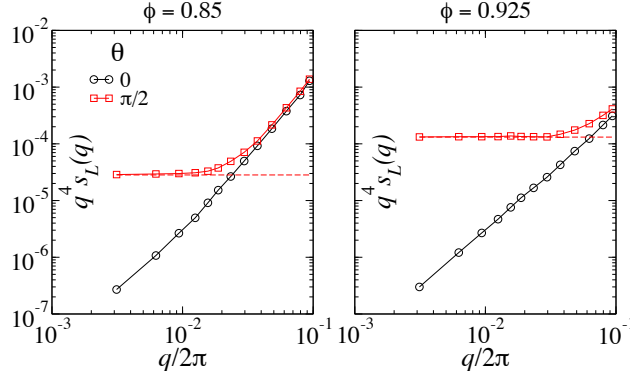
Figure 3.3: $q^4 s_L(q)$ for cuts along the axis at $\theta = 0$ and $\theta = \pi/2$ at $\phi = 0.85$ (left) and $\phi = 0.925$ (right) compared with the continuum solution (dashed lines).

squares in the Fig. 3.4).

Now let us compare $s_L(\mathbf{q})$ at $\theta = \pi/2$ and $s_T(\mathbf{q})$ at $\theta = 0$ to their continuum expressions. At low q (long wave length), the actual response compares well with the continuum solution (dashed curves) – with both showing q^{-4} behavior for small wave numbers. For large wave numbers, however, the predictions become bad. The validity range of linear elasticity extends out to a larger q (smaller wave length) at $\phi = 0.925$ (right) than $\phi = 0.85$ (left) for both longitudinal and transverse structure factors. In other words, elasticity is only valid at very long wave length limit near jamming.

For simplicity, we compute the angle independent structure factors $s_L(q)$ and $s_T(q)$ as the following: $\log s_L(q) = \langle \log s_L(\mathbf{q}) \rangle_\theta$ and $\log s_T(q) = \langle \log s_T(\mathbf{q}) \rangle_\theta$ where $\langle \rangle_\theta$ denotes averages over θ. We define the scaled structure factors as

$$
\begin{aligned}
S_L(q) &= \frac{s_L(q)}{s_L^{\text{cont}}(q)}, \\
S_T(q) &= \frac{s_T(q)}{s_T^{\text{cont}}(q)},
\end{aligned}
\tag{3.6}
$$

41
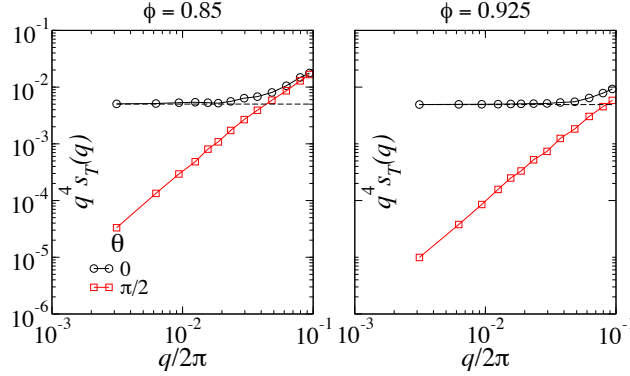
Figure 3.4: $q^4 s_T(q)$ for cuts along the axis at $\theta = 0$ and $\theta = \pi/2$ at $\phi = 0.85$ (left) and $\phi = 0.925$ (right) compared with the continuum solution (dashed lines).

for $q \neq 0$. Here $s_L^{\text{cont}}(q)$ and $s_T^{\text{cont}}(q)$ are the isotropic continuum predictions [3].

The angle-averaged scaled structure factors $S_L(q)$ and $S_T(q)$ measured for different ϕ are shown in Fig. 3.5. Qualitatively similar behavior is found for $S_L(q)$ and $S_T(q)$ at various packing fractions: they start at very high values for large q, go down as q decreases, and finally asymptote to unity as $q \to 0$ – which implies that elasticity works perfectly in that limit. This q-dependent form is more pronounced in the longitudinal mode than it is in the transverse mode. We find that the crossover to the linear elastic behavior at low q is strongly controlled by the distance to jamming –set by ϕ. It should be also noted that $S_T(q)$ does not look as sensitive to jamming as $S_L(q)$ does.

In Fig. 3.6, we show that the data can be made to collapse for various ϕ when plotting $S_L(q)$ versus $\langle p \rangle^{-0.4} q/2\pi$ and $S_T(q)$ versus $\langle p \rangle^{-1/4} q/2\pi$. Here

---

[3]We did an isotropic averaging in log space, i.e. $\log |u_T^{\text{cont}}(q)|^2 = \frac{1}{\pi} \int_0^\pi \log |u_T^{\text{cont}}(q, \theta)|^2 d\theta$ which leads to $|u_T^{\text{cont}}(q)|^2 = F^2/4\mu^2 q^4 V^2$. Note that $\log |u_T^{\text{cont}}(q, \theta)|^2$ is not finite at $\theta = \pi/2$ but the integral is bounded.
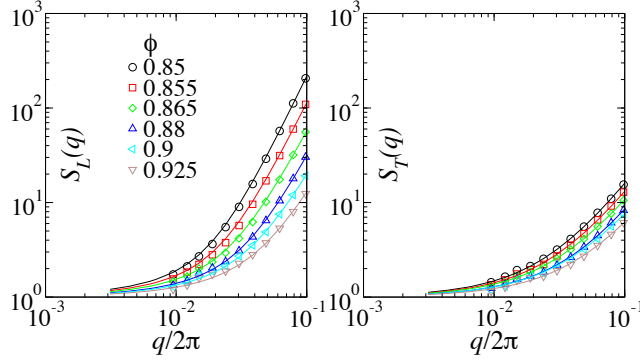
Figure 3.5: $S_L(q)$ versus $q/2\pi$ (left) and $S_T(q)$ versus $q/2\pi$ (right) for different ϕ.

the crossover length scale between elastic and non-elastic regimes – say ξ_L and ξ_T for the longitudinal and transverse modes – are proportional to $\xi_L \propto \langle p \rangle^{-0.4}$ and $\xi_T \propto \langle p \rangle^{-1/4}$. These scalings are consistent with divergence at jamming transition.

Let us summarize this section: study of the elastic Green's function in q-space exhibits a crossover, denoted by length ξ, to the classical elasticity solution in small wave numbers. ξ diverges at jamming in the form of a power law with different exponents for the longitudinal and transverse modes; ξ_L has a larger exponent than ξ_T does (in an absolute sense) meaning that jamming is more pronounced in longitudinal motion. The transverse displacements, however, become infinitely large near jamming, as $\mu \to 0$ and K remains finite [4]. It is evident from Eq. (3.3) that K/μ sets the ratio between the transverse and longitudinal components. Despite this, it is $S_L(q)$ that is more sensitive to jamming.

---

[4]We discuss the scalings of μ and K with $\langle p \rangle$ in Section 3.3
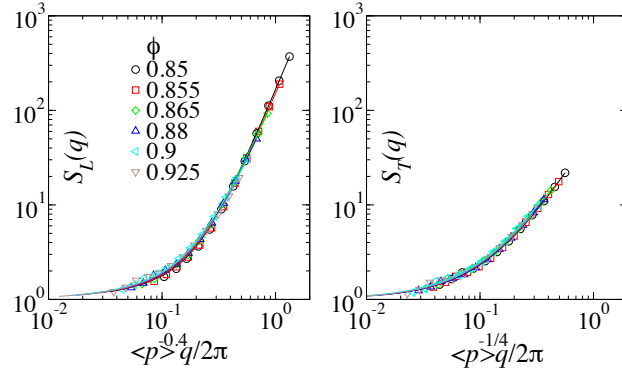
Figure 3.6: $S_L(q)$ versus $\langle p \rangle^{-0.4} q/2\pi$ (left) and $S_T(q)$ versus $\langle p \rangle^{-1/4} q/2\pi$ (right) for different ϕ.

3.3 Local Elasticity

The presence of disorder in an amorphous matter gives rise to strong fluctuations in the local elastic constants particularly at small scales. As discussed in Section 3.2, linear isotropic homogeneous elasticity assumes that these heterogeneities are negligible. In fact, the severe non-continuum behavior observed in the point response – which is intensified near jamming – is due to the inherent spatial non-homogeneities in the structure of elastic moduli. This gives us at least one important reason to study local elastic properties of amorphous structures as in [55]. Tsamados et al. [50] attempted to associate a characteristic scale to the elastic heterogeneities by measuring the local elastic properties at different coarse-graining sizes. They found a characteristic length of five interatomic distances, but a systematic study of modulus fluctuations with respect to proximity to jamming was lacking in their work. A similar study has been performed in [37] to measure spatial distributions of the local moduli in glasses without identifying any interesting size.

As opposed to the previous studies, in this work, our focus will be based on the scale dependence of average shear modulus and not the spatial fluctuations. We use a systematic coarse-graining approach and monitor the convergence of shear modulus value toward its bulk limit. The scale dependence of the local shear modulus is quantified by applying homogeneous shear strain using no slip boundary conditions with boxes of various size, R. The applied constraints at the boundaries prevent non-affine relaxations which result in the increased shear modulus beyond its fully relaxed value. Response to the elastic wave perturbation is also studied in order to measure

the average elastic constant and characterize its potential dependence on the incident wave.

3.3.1 Constrained Homogeneous Shear

The local elastic constants are usually interpreted to have the same meaning as the bulk quantity, typically defined in the context of continuum mechanics. The local elasticity tensor relates the changes in the local stress tensor to an applied uniform strain in an elastic material. The local Born shear modulus $\mu_{\mathrm{Born}}(\mathbf{r}_i)$ may be computed by carrying out a summation over all pairs of interacting particles j with particle i [as in Eq. (B.2)]. The bulk Born shear modulus μ_{Born} – derived in Appendix B.1 – is simply the spatial average of $\mu_{\mathrm{Born}}(\mathbf{r}_i)$, i.e. $\mu_{\mathrm{Born}} = \langle \mu_{\mathrm{Born}}(\mathbf{r}_i) \rangle$. In order to define the *net* local shear modulus locally in a sub-region $\Omega \in V$, Eq. (3.11) may be solved with all exterior particles held *fixed*, i.e. $\delta u_{i\alpha} = 0$, and the local moduli then can be defined. The main assumption is that while the interior particles can move nonaffinely, the exterior particles act as fixed, rigid boundaries.

Now let us simply divide the simulation cell into squares of varying length R and follow the above procedure for each box to find a coarse-grained shear modulus $\mu(\mathbf{r}_i, R)$. The local *correction* shear modulus is defined as $\mu_c(\mathbf{r}_i, R) = \mu_{\mathrm{Born}}(\mathbf{r}_i) - \mu(\mathbf{r}_i, R)$ and its spatial average is $\mu_c(R) = \langle \mu_c(\mathbf{r}_i, R) \rangle$. We plot $\mu(R)$ – which is a spatial average $\mu(R) = \langle \mu(\mathbf{r}_i, R) \rangle$ – against R in Fig. 3.7 left exhibiting significant size dependence. At the shortest length-scales $R \ll L$, where no inhomogeneous correction is allowed because most of the particles lie on the perimeter and move affinely, $\mu_c(R) \approx 0$ or
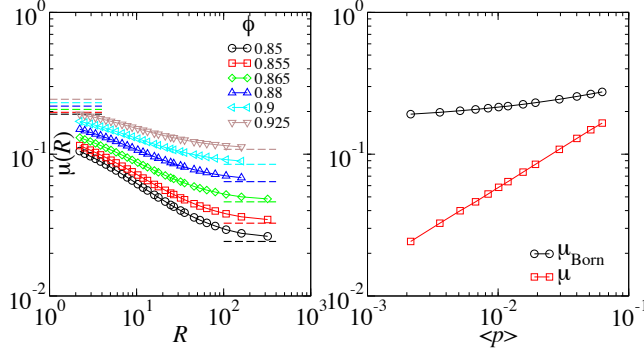
Figure 3.7: Shear modulus $\mu(R)$ plotted against R at different ϕ (left) and Scaling of μ_{Born} and μ with $\langle p \rangle$ (right). The dashed lines (left) illustrate the asymptotic behavior at small R $[\mu(R) \to \mu_{\text{Born}}]$ and large R $[\mu(R) \to \mu]$.

$\mu(R) \approx \mu_{\text{Born}}$. In fact, for small squares the contribution of particles at and near the surface becomes more dominant. At longer length-scales, $\mu(R)$ decreases monotonically toward the true global value for these periodic systems, $\mu = \mu(R \to \infty)$, as increasingly longer wavelength inhomogeneous corrections are allowed to $\mu(R)$ and the contribution of the bulk particles increases compared to the Born term μ_{Born} which is scale independent.

Figure 3.7 right illustrates the pressure dependence of μ_{Born} and μ. Near jamming, μ decreases toward zero, as the contribution of the correction term $\mu_c = \mu_c(R \to \infty)$ grows relative to the Born term μ_{Born} which does not look so sensitive to $\langle p \rangle$.

From the assumption that particles move only affinely on the perimeter of the box, one can estimate that $\mu_c(R) \propto N_{\text{Bulk}}/N$ where N is the total number of particles in a square of length R and N_{Bulk} is the number of particles in the bulk. The number of particles on the perimeter, which we denote by N_{Perim}, is proportional to R. Now $N_{\text{Bulk}} = N - N_{\text{Perim}}$ and we have that $N \propto R^2$.
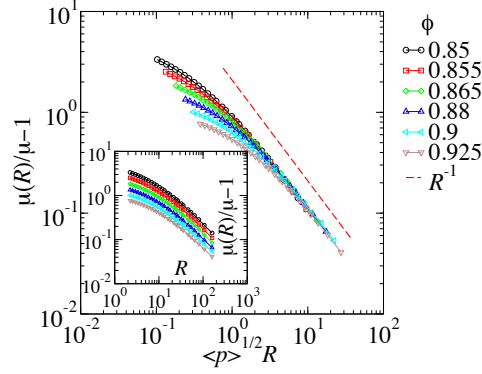
Figure 3.8: $\mu(R)/\mu - 1$ plotted against $\langle p \rangle^{1/2}R$ at different ϕ. In the inset, $\mu(R)/\mu - 1$ versus R is shown. The dashed line shows R^{-1}.

Hence $\mu_c(R) = \mu_c(1 - \xi/R)$ where ξ has dimension of length and determines how quickly $\mu_c(R)$ should reach its asymptote μ_c. Upon using this relation, we obtain the following formula for $\mu(R)$ with an explicit dependence on R (and of course $\langle p \rangle$)

$$\mu(R) = \mu + \mu_c \frac{\xi}{R}. \tag{3.7}$$

Now, $\xi\mu_c/\mu$ is a characteristic length which is the R above which one almost recovers the true global modulus; namely $\mu(R > \frac{\mu_c}{\mu}\xi) \approx \mu$. Evidently(see Fig. 3.7 left) this special size scales with $\langle p \rangle$. In Fig. 3.8, we show that the data can be made to collapse (at large R!) for various ϕ when plotting $\mu(R)/\mu - 1$ versus $\langle p \rangle^{\frac{1}{2}}R$. The theory seems to capture the fact that R^{-1} regime is clearly reached at large values of R (see the tails in the inset). However, at low R (say $R < 10$) the discrepancy can be due to the fact that $\mu(R) \approx \mu_{\text{Born}}$. Physically speaking, the sample size R needed to converge to the fully relaxed shear modulus diverges as $\langle p \rangle^{-1/2}$ which is close to the $\xi_L \sim \langle p \rangle^{-0.4}$ result discussed in Section 3.2.

3.3.2 Elastic Wave Response

Response to plane wave forcing with a varying wavelength is used to quantify the scale dependence in the shear modulus. We perturb the system with an external force vector $F_{i\alpha}^{\text{ext}} = F\psi_{i\alpha}$ in the form of an ordinary unit transverse plane wave where $\psi_{j\alpha} = n_\alpha^\perp e^{i\mathbf{q}'\cdot\mathbf{r}_j}/\sqrt{N}$. Here $\mathbf{q}'$ is the wave vector with wave number q' and $\mathbf{n}^\perp = \mathbf{q}'^\perp/q'$ is the unit polarization vector. We solve $H_{i\alpha j\beta}\, u_{j\beta} = F\psi_{i\alpha}$ to find the response. The affine displacements is denoted by $X_{\text{aff}}\psi_{i\alpha}$ where X_{aff} represents their magnitude. Given $u_{i\alpha} = \delta u_{i\alpha} + X_{\text{aff}}\psi_{i\alpha}$ and upon replacing it in the linear response equation, we obtain

$$H_{i\alpha j\beta}\, \delta u_{j\beta} = F_{i\alpha}^{\text{ext}} - X_{\text{aff}}H_{i\alpha j\beta}\psi_{j\beta}. \qquad (3.8)$$

The affine displacement magnitude X_{aff} in response to the perturbing force may be obtained by solving Eq. (3.8) using $\delta u_{i\alpha} = 0$

$$X_{\text{aff}} = F/(\psi_{i\alpha}H_{i\alpha j\beta}\psi_{j\beta}). \qquad (3.9)$$

Typical snapshots of the force field $F_{i\alpha}^{\text{ext}}$ and nonaffine displacements $\delta u_{i\alpha}$ calculated from Eq. (3.8) are depicted in Fig. 3.9.

We turn now to the calculation of the elastic coefficient μ using the elastic wave response. See Appendix B.2 where we obtain a relation between the energy change $\Delta\mathcal{U}$ and the elastic constant. We find

$$\mu(q') = \langle p \rangle + F^2[\Delta\mathcal{U}(q')\, q'^2 V/N]^{-1}. \qquad (3.10)$$

The change in energy of the affine state is given by $\Delta\mathcal{U}_{\text{aff}} = \frac{1}{2}X_{\text{aff}}^2\psi_{i\alpha}H_{i\alpha j\beta}\psi_{j\beta}$.

49
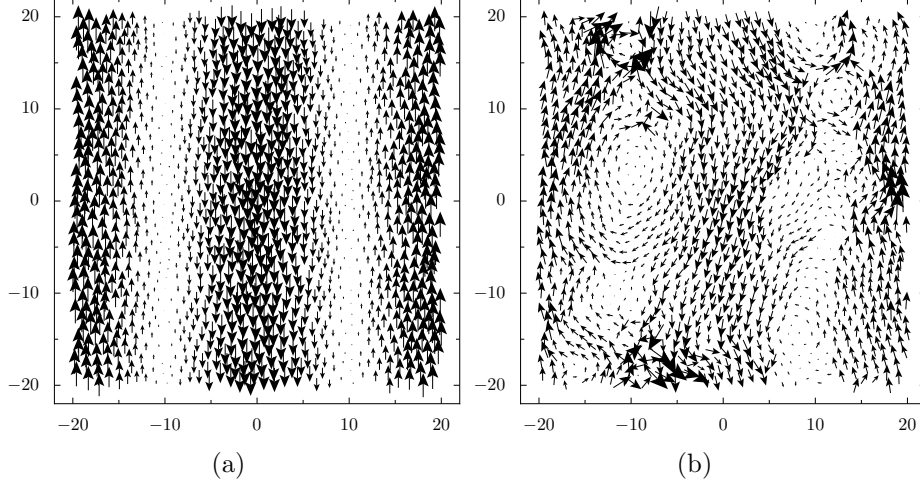
Figure 3.9: The force field $F_{i\alpha}^{\text{ext}}$ with a plane wave structure (a) and the corresponding response $u_{i\alpha}$ (b).

Inserting Eq. (3.9) leads to $\Delta\mathcal{U}_{\text{aff}} = \frac{1}{2}F^2/(\psi_{i\alpha}H_{i\alpha j\beta}\psi_{j\beta})$, while the energy change of the final state is given by $\Delta\mathcal{U} = \frac{1}{2}F^2(\psi_{i\alpha}H_{i\alpha j\beta}^{-1}\psi_{j\beta})$. We have $\Delta\mathcal{U} = \Delta\mathcal{U}_{\text{aff}}$ when and only when $\psi_{i\alpha}$ is along an eigenvector of $H_{i\alpha j\beta}$.

Our results for the shear moduli $\mu(\lambda)$ as a function of the wavelength of the applied elastic wave $\lambda = 2\pi/q'$ are collected in Fig. 3.10 left. It looks like there is not so much scale dependence, as $\mu(\lambda)$ hits the plateau at rather small λ – which is *insensitive* to jamming. In in Fig. 3.10 right, the quantity $1 - \mu(\lambda)/\mu$ decays almost as λ^{-2} with a pre-factor that is independent of ϕ (see the rescaled data by λ^{-2} in the inset). This scaling behavior is simply what would be seen for a phonon dispersion at high q values.

We close this section by concluding that the wave method will not reveal any interesting characteristic length. The non-affine corrections to the affine displacements reduce $\mu_{\text{aff}}(\lambda)$ [5] to $\mu(\lambda)$ but not in an interesting fashion!

---

[5]Upon replacing $\mathcal{U}$ with $\mathcal{U}_{\text{aff}}$ in Eq. (3.10), we obtain an expression for $\mu_{\text{aff}}(\lambda)$.
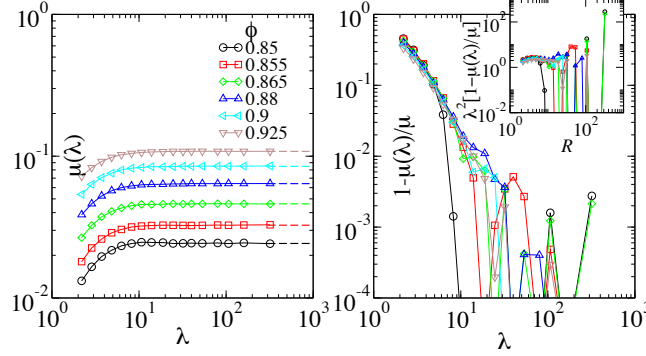
Figure 3.10: Dependence of the shear modulus $\mu(\lambda)$ (left) and the relative error on the shear modulus $1 - \mu(\lambda)/\mu$ (right) on the wavelength $\lambda = 2\pi/q'$ for various ϕ. The inset is the same as the main plot but rescaled by λ^2. The dashed lines represent μ.

$\mu_{\text{aff}}(\lambda)$ differs from $\mu(\lambda)$ only by a scale factor (not shown here). The weak λ dependence is simply due to the dispersion effect which manifest itself at small λ values [6]. However, in the box method these corrections exhibit a strong scale dependence, as particles are pinned on the boundary while the wave method does not pin any particles.

---

[6] Assuming that the eigenmodes of the Hessian can be approximated as plane waves and the associated eigenvalues scale as $sin^2 q$, we obtain $\Delta \mathcal{U} \propto 1/sin^2 q$. Using Eq. (B.9), we have $\mu \propto sin^2 q/q^2$. In the long wave-length limit, i.e. $q \to 0$, μ reaches a plateau, and for a large q, i.e. $sin^2 q \to 1$, $\mu \propto q^{-2}$.

3.4   Response To a Bulk Deformation

Existence of nonaffine linear displacements of amorphous packings subject to a macroscopic uniform strain is a direct consequence of disorder, which itself leads to spatial fluctuations in elastic properties. In the Fourier decomposition of their nonaffine displacement field, Leonforte et al. [21, 23] observed that the longitudinal and transverse powers are proportional to q^{-2} with no indication of any special wave number. One important question is that to what extent the observed behavior in Green's function, discussed in previous section, carries over to this form of driving. In this section, we investigate the nonaffine displacement field using a *unconstrained* homogeneous strain applied to a periodic cell. We focus on two modes of global deformation here which are isotropic compression and pure shear.

3.4.1   Nonaffine Response

Macroscopic deformations of the sample are performed by changing the shape of the periodic box via the deformation gradient tensor $F_{\alpha\beta}$. Changes in $F_{\alpha\beta}$ correspond to affine transformations of all the particles following the cell shape. At zero temperature, an infinitesimal deformation of the system is often performed in two steps. First, starting from a local minimum, the particle coordinates affinity follow the change of the cell coordinate. The real space position of particle i is thus mapped from $r_{i\alpha}$ to $F_{\alpha\beta}r_{i\beta}$. Second the particles are allowed to relax to the nearest equilibrium position $r_{i\alpha}$, with $F_{\alpha\beta}$ being fixed. The nonaffine part of the deformation is then characterized by $\delta u_{i\alpha} = u_{i\alpha} - u_{i\alpha}^{\text{aff}}$ where $u_{i\alpha}^{\text{aff}} = (F_{\alpha\beta} - \delta_{\alpha\beta})r_{i\beta}$.

For now, let us move on to how we may derive these nonaffine fields in response to some prescribed mode of deformation parametrized by $F_{\alpha\beta}$. The equation of motion for $\delta u_{i\alpha}$ is obtained by solving [20]

$$H_{i\alpha j\beta} \, \frac{\delta u_{j\beta}}{\eta_{\sigma\gamma}} = \Xi_{i\alpha}^{\sigma\gamma}, \qquad (3.11)$$

where $\eta_{\alpha\beta} = (F_{\gamma\alpha}F_{\gamma\beta} - \delta_{\alpha\beta})/2$ is the Lagrangian strain tensor and $\Xi_{i\alpha}^{\beta\gamma} = -\partial^2 \mathcal{U}/\partial r_{i\alpha}\partial\eta_{\beta\gamma}|_{\eta_{\beta\gamma}\to 0}$ is the field of forces which results from an affine deformation of all the particles. The above equation shows that $\delta u_{i\alpha}$ is just the linear response to these extra forces under deformation along $\eta_{\alpha\beta}$.

For a given relaxed configuration, $\Xi_{i\alpha}^{\sigma\gamma}$ is first computed, and we, then, solve for $\delta u_{i\alpha}$ numerically using the sparse matrix routines in the SciPy library. We have checked that this procedure gives agreement with the less precise procedure of applying a small finite deformation and performing a subsequent energy minimization in LAMMPS. Examples for the field $\delta u_{i\alpha}$ in isotropic compression $\eta_{\alpha\beta} = \epsilon\delta_{\alpha\beta}$ and pure shear $\eta_{\alpha\beta} = \epsilon(\delta_{\alpha x}\delta_{\beta x} - \delta_{\alpha y}\delta_{\beta y})$ are shown in Figs. 3.11 and 3.12 for $\phi = 0.85$ and $\phi = 0.925$. Here ϵ is an infinitesimal strain. The spatial structure of these displacements will be discussed below.

3.4.2 Nonaffine Displacements Decomposition

Here we discuss the Fourier longitudinal and transverse structure factors, $s_L(\mathbf{q})$ and $s_T(\mathbf{q})$ of nonaffine displacement field in response to compression and shear as we did for the point response in Section 3.2.3. The nonaffine displacements, computed from Eq. (3.11), are interpolated on a fine grid and
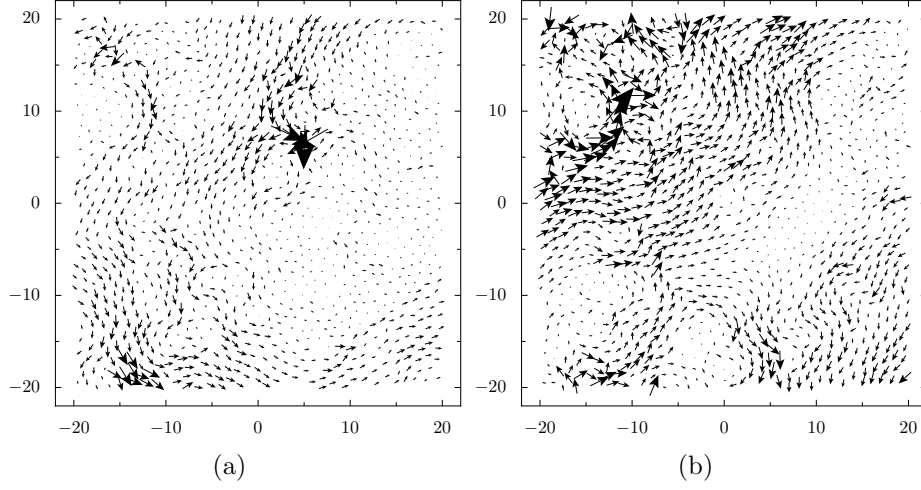
Figure 3.11: $\delta u_{i\alpha}$ field in isotropic compression (a) and pure shear (b) for $\phi = 0.85$.
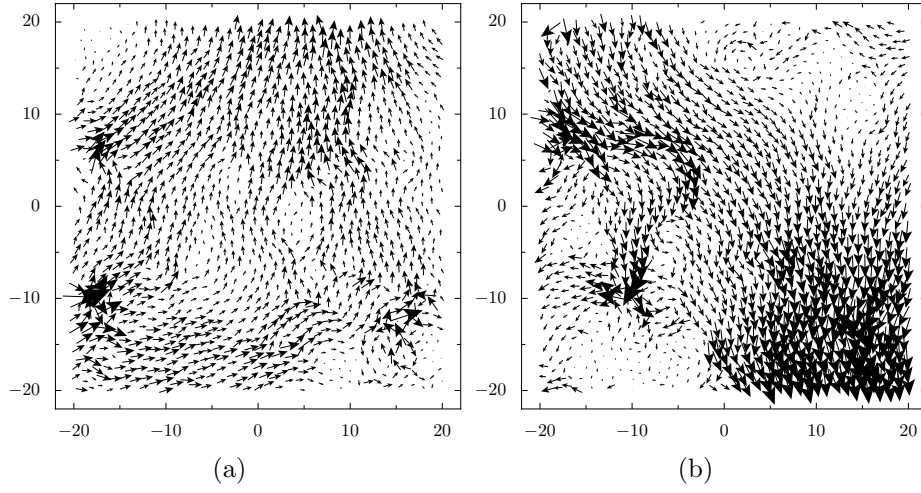

Figure 3.12: $\delta u_{i\alpha}$ field in isotropic compression (a) and pure shear (b) for $\phi = 0.925$.

DFT is performed subsequently.

From a continuum perspective, the nonaffine elastic response may be expressed as that of an isotropic homogeneous linear elastic medium perturbed by local force dipoles with varying magnitudes and angles [33]. Now let us assume that these dipoles can be expressed as q in an average sense. We showed in Section 3.2 that the average elastic Green's function scales as q^{-2} in long wave length limit for an amorphous system. Thus, given that the response is described as the product between the Green's function and applied force, we obtain the q^{-1} scaling, for the amplitude, which is expected to be valid at small q values.

In Fig. 3.13, the ensemble averaged structure factors are rescaled by q^{-2} at $\phi = 0.85$. We display $s_L^c(\mathbf{q})$ and $s_T^c(\mathbf{q})$ computed in compression (left) and $s_L^s(\mathbf{q})$ and $s_T^s(\mathbf{q})$ in shear (right). Our first observation is that $s_L^c(\mathbf{q})$ and $s_T^c(\mathbf{q})$ are not so sensitive to θ. $s_L^s(\mathbf{q})$ and $s_T^s(\mathbf{q})$, however, are strongly angle dependent especially at low q values.

Looking at the real space correlations gives us a better insight toward the observed anisotropy in $s_L^s(\mathbf{q})$ and $s_T^s(\mathbf{q})$. The real space volumetric strain field $\Phi(\mathbf{r}_j) = \nabla.\mathbf{u}$ and vorticity field $\omega(\mathbf{r}_j) = \nabla \times \mathbf{u}$ can be obtained by taking an inverse discrete Fourier transform of $u_L(\mathbf{q})$ and $u_T(\mathbf{q})$

$$
\begin{aligned}
\Phi(\mathbf{r}_j) &= \frac{1}{N_g} \sum_{\mathbf{q}} u_L(\mathbf{q}) e^{i\mathbf{q}\cdot\mathbf{r}_j}, \\
\omega(\mathbf{r}_j) &= \frac{1}{N_g} \sum_{\mathbf{q}} u_T(\mathbf{q}) e^{i\mathbf{q}\cdot\mathbf{r}_j}.
\end{aligned}
\tag{3.12}
$$

We also check that finite difference in real space gives identical results except

(a) $q^2 s_L^c(\mathbf{q})$

(b) $q^2 s_L^s(\mathbf{q})$

(c) $q^2 s_T^c(\mathbf{q})$
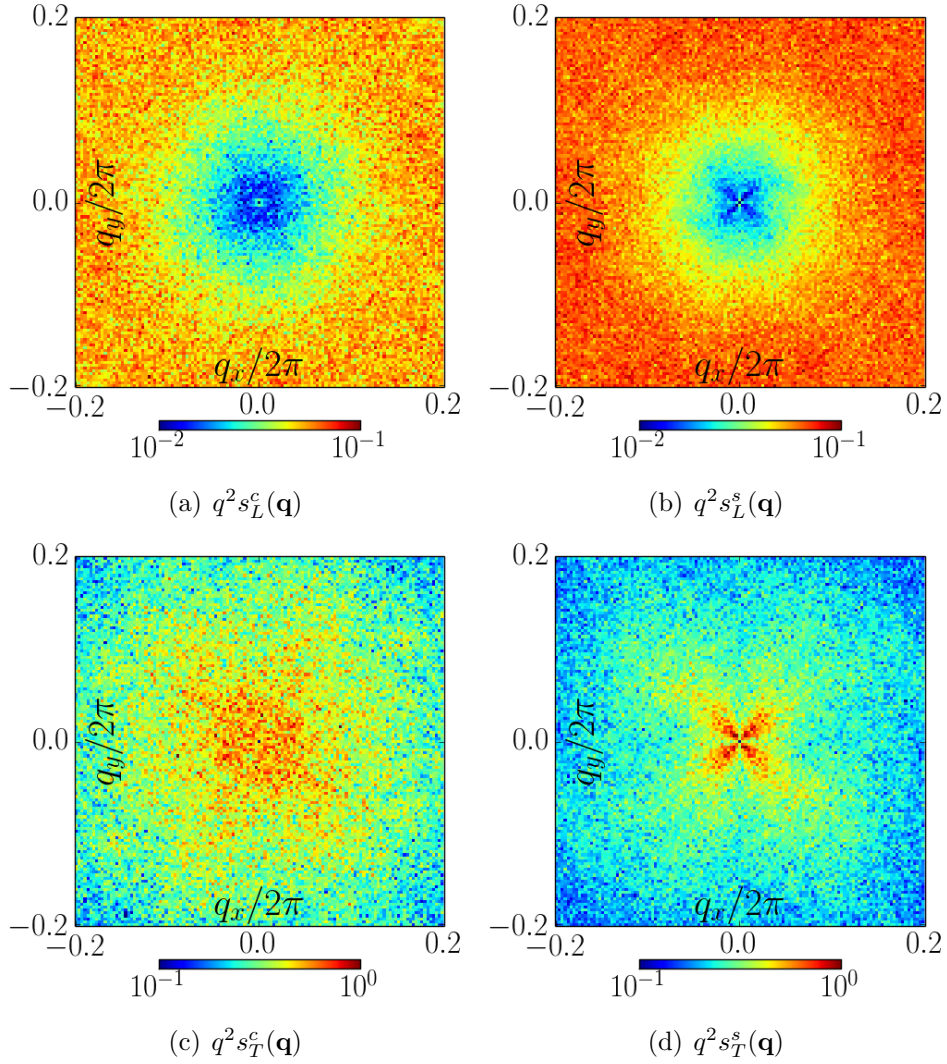
(d) $q^2 s_T^s(\mathbf{q})$

Figure 3.13: Maps of longitudinal (top) and transverse (bottom) structure factors in compression (left) and shear (right) plotted for $\phi = 0.85$ using a decimal log scale.

56

at tiny q.

Figure 3.14 shows $\Phi_c(\mathbf{r}_i)$ and $\omega_c(\mathbf{r}_i)$ (subscript c denotes compression) at left and $\Phi_s(\mathbf{r}_i)$ and $\omega_s(\mathbf{r}_i)$ (subscript s denotes shear) at right for a single realization at $\phi = 0.85$. Long range, highly anisotropic spatial correlations are evident for $\omega_s(\mathbf{r}_i)$ in Fig. 3.16(d) which localizes at roughly macroscopic maximum *global* shear planes along the diagonals. We also observe these features for $\Phi_s(\mathbf{r}_i)$ in Fig. 3.16(b) but to a lesser degree. $\Phi_c(\mathbf{r}_i)$ and $\omega_c(\mathbf{r}_i)$ have no directional preference, as seen in Fig. 3.16(a) and (c).

Figures 3.20 and 3.16 are the same as Figs. 3.13 and 3.14 but generated for $\phi = 0.925$. One difference in Fourier space pictures is the fact that $q^2 s_L^c(\mathbf{q})$ in Fig. 3.20(a) is almost flat, and that differs from what we see in the loose packing in Fig. 3.13(a).

To quantify these correlations in compression, we calculate the angle dependent structure factors $s_L^c(q)$ and $s_T^c(q)$ as the following: $\log s_L^c(q) = \langle \log s_L^c(\mathbf{q}) \rangle_\theta$ and $\log s_T^c(q) = \langle \log s_T^c(\mathbf{q}) \rangle_\theta$ where $\langle \rangle_\theta$ denotes averages over θ. These quantities are plotted in Fig. 3.17 for various ϕ. We make several important points here. First, $s_L^c(q)$ shown in Fig. 3.17(a) looks much more sensitive to jamming than $s_T^c(q)$ does in Fig. 3.17(b), which is consistent with the Green's function behavior discussed in Section 3.2. Secondly, the low-q values of $s_T^c(q)$ almost decay as q^{-2} [the plateau of $q^2 s_T^c(q)$ in Fig. 3.17(b)], while the tail of $q^2 s_T^c(q)$ for high-q values indicates a faster decay than q^{-2}. Far away from the jamming transition, $s_L^c(q)$ almost follows q^{-2} scaling [the brown downward triangles in Fig. 3.17(a)]. As we approach jamming, however, we observe large deviations from the q^{-2} behavior at intermediate q where the decay gets very slow, which is in agreement with non-continuum

(a) $\Phi_c(\mathbf{r}_i)$

(b) $\Phi_s(\mathbf{r}_i)$

(c) $\omega_c(\mathbf{r}_i)$

(d) $\omega_s(\mathbf{r}_i)$

Figure 3.14: Real space images of $\Phi(\mathbf{r}_i)$ (top) and $\omega(\mathbf{r}_i)$ (bottom) generated for compression and shear at $\phi = 0.85$.

58

(a) $q^2 s_L^c(\mathbf{q})$

(b) $q^2 s_L^s(\mathbf{q})$

(c) $q^2 s_T^c(\mathbf{q})$

(d) $q^2 s_T^s(\mathbf{q})$
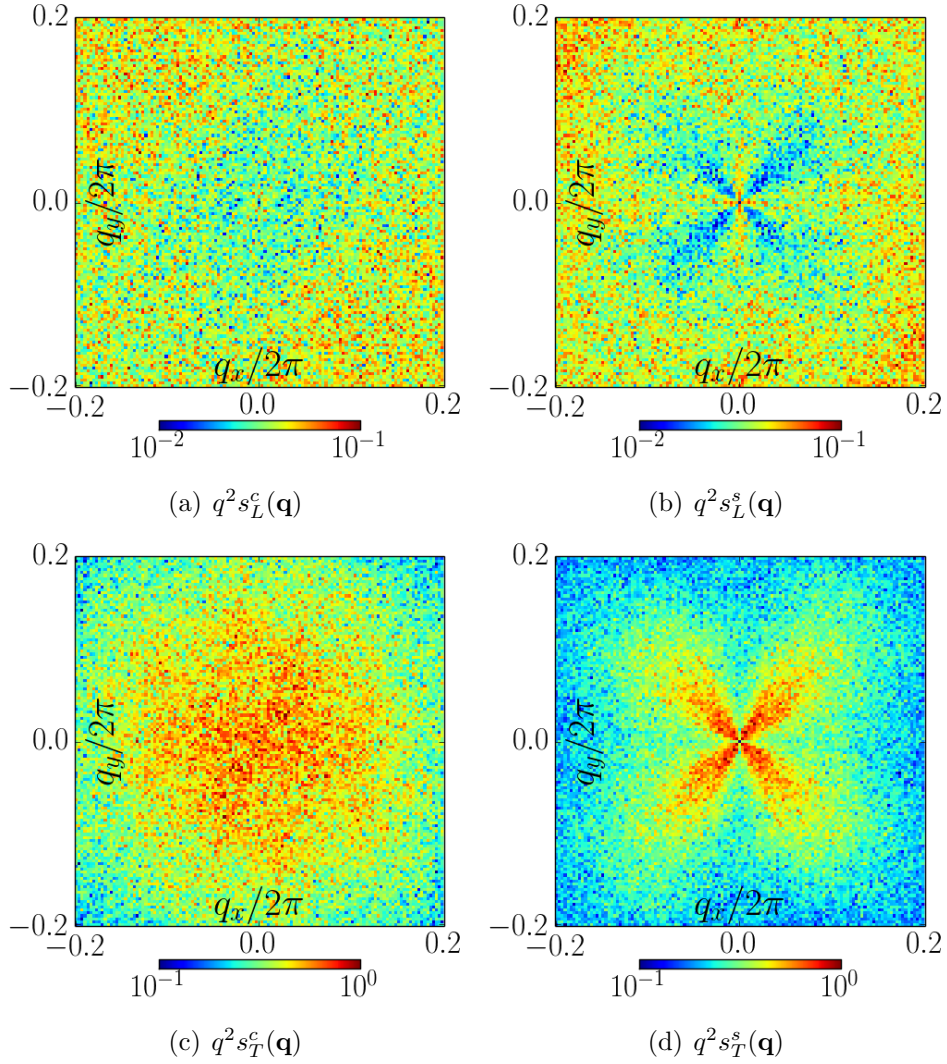
Figure 3.15: Maps of longitudinal (top) and transverse (bottom) structure factors in compression (left) and shear (right) plotted for $\phi = 0.925$ using a decimal log scale.

59

(a) $\Phi^c(\mathbf{r}_i)$

(b) $\Phi^s(\mathbf{r}_i)$

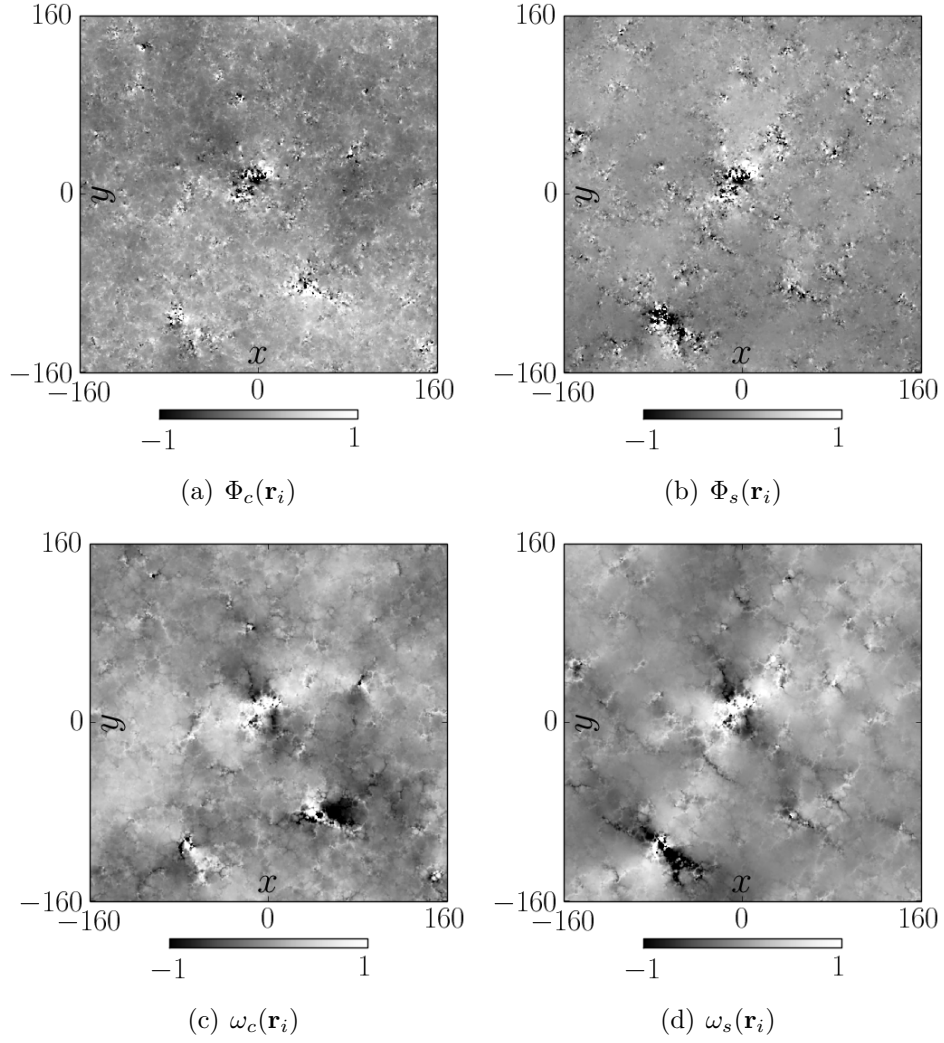(c) $\omega^c(\mathbf{r}_i)$

(d) $\omega^s(\mathbf{r}_i)$
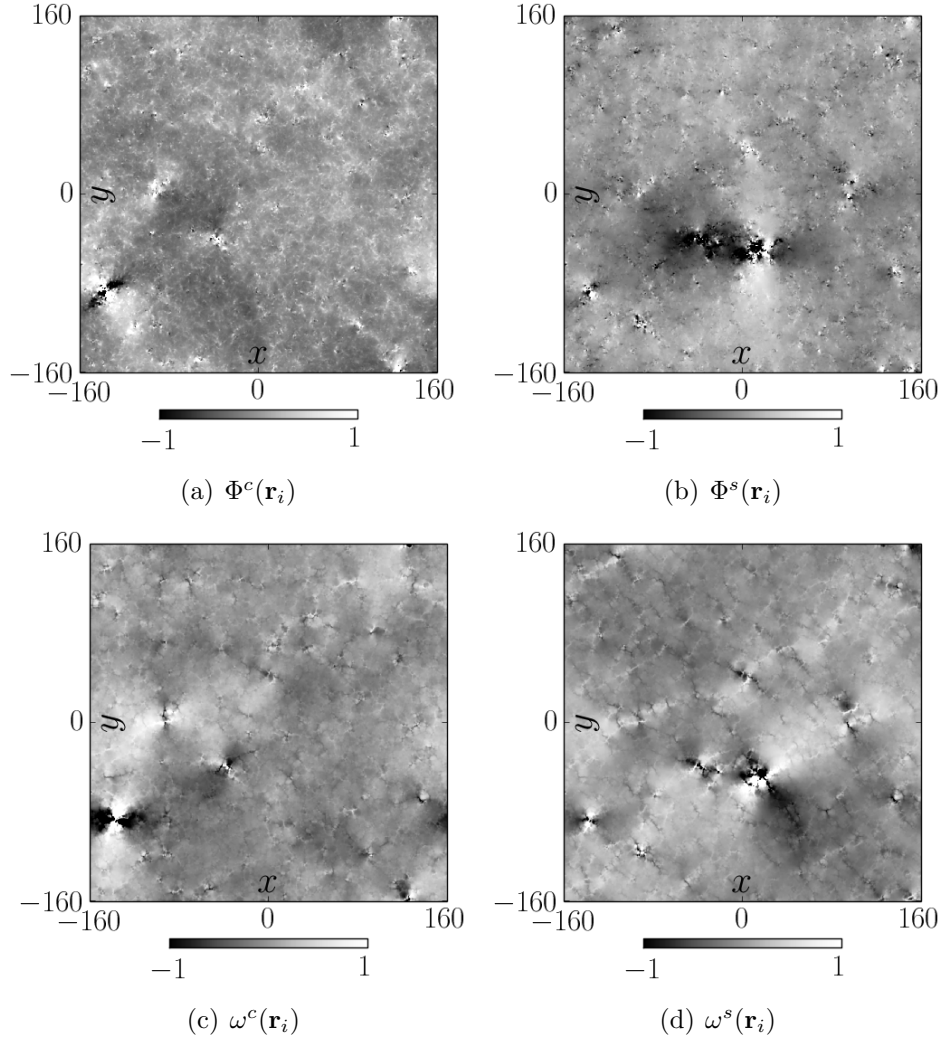
Figure 3.16: Real space images of $\Phi(\mathbf{r}_i)$ (top) and $\omega(\mathbf{r}_i)$ (bottom) generated for compression and shear at $\phi = 0.925$.

Figure 3.17: $q^2 s_L^c(q)$ versus $q/2\pi$ (a) and $q^2 s_T^c(q)$ versus $q/2\pi$ (b) for different ϕ in *compression*. In the insets, $s_L^c(q)$ and $s_T^c(q)$ are plotted against $q/2\pi$.

behavior observed in Section 3.2.

We now quantify the anisotropic shear correlations. The structure factors $s_L^s(\mathbf{q})$ and $s_T^s(\mathbf{q})$ measured along $\theta = 0$ –the axis– and $\theta = \pi/4$ –the diagonal– at $\phi = 0.85$ are shown in Fig. 3.18. It should be noted that these values were calculated by binning according to $\log q$ along these two directions. Both $s_L^s(\mathbf{q})$ and $s_T^s(\mathbf{q})$ show anisotropy at low-q values – long wavelength – due to an anisotropic deformation at boundaries. In contrast, large wave numbers
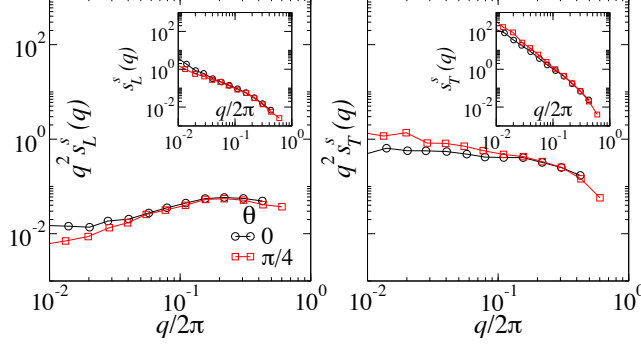
Figure 3.18: $q^2 s_L^s(q)$ (left) and $q^2 s_T^s(q)$ for cuts along the axis at $\theta = 0$ and $\theta = \pi/4$ at $\phi = 0.85$. The insets plot $s_L^s(q)$ and $s_T^s(q)$.

are not so sensitive to bulk deformation and $s_L^s(\mathbf{q})$ and $s_T^s(\mathbf{q})$ become nearly angle-independent. Nature of low-q anisotropy is different for $s_L^s(\mathbf{q})$ and $s_T^s(\mathbf{q})$. At $\theta = \pi/4$, $s_T^s(\mathbf{q})$ is largest, while $s_L^s(\mathbf{q})$ is smallest. Along the axis, the trend is opposite; namely $s_T^s(\mathbf{q})$ is smallest and $s_L^s(\mathbf{q})$ is largest.

Figure 3.19 plots the same data as above but for $\phi = 0.925$. The data qualitatively agrees with that of $\phi = 0.925$ except that $q^2 s_L^s(\mathbf{q})$ becomes nearly independent of q.

The angle-averaged structure factors $s_L^s(q)$ and $s_T^s(q)$ measured for different ϕ are shown in Fig. 3.20, which compare well with those measured in compression as in Fig. 3.13.

We conclude that the basic picture of force dipoles acting in an uncorrelated way on a homogeneous elastic sheet holds. However, there are important departures from this picture.While the longitudinal mode is sensitive to distance from point J, the transverse component is almost insensitive. Mode of applied deformation at boundaries can largely impact vorticity and volumetric strain at large wavelengths. In pure shear, we observed enhanced
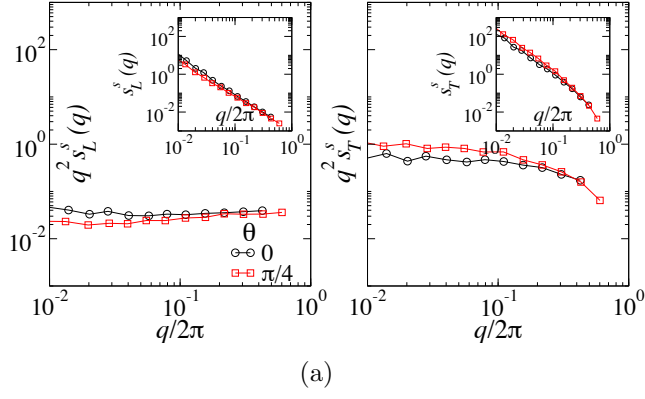
Figure 3.19: $q^2 s_L^s(q)$ (left) and $q^2 s_T^s(q)$ for cuts along the axis at $\theta = 0$ and $\theta = \pi/4$ at $\phi = 0.925$. The insets plot $s_L^s(q)$ and $s_T^s(q)$.

vorticity power along the diagonal. Also, volumetric strain shows this property along the axes.
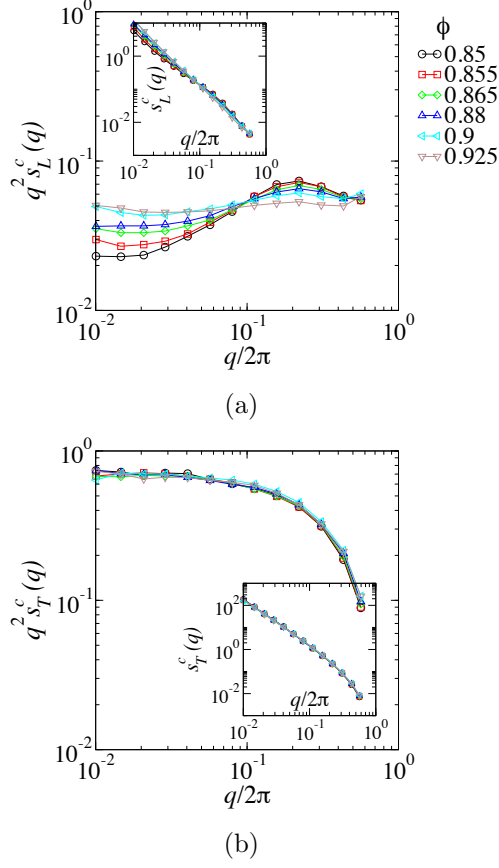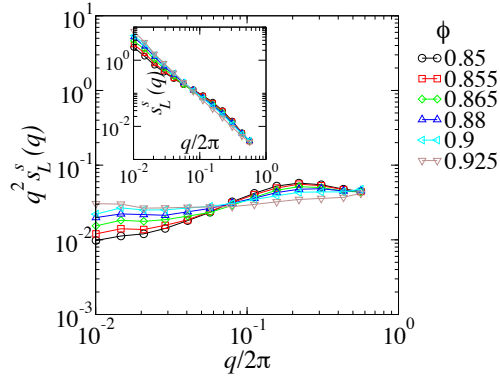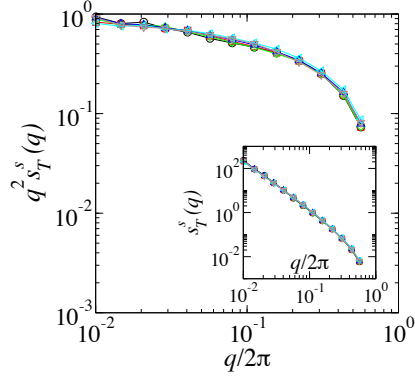
Figure 3.20: $q^2 s_L^s(q)$ versus $q/2\pi$ (a) and $q^2 s_T^s(q)$ versus $q/2\pi$ (b) for different ϕ in *shear*. In the insets, $s_L^s(q)$ and $s_T^s(q)$ are plotted against $q/2\pi$.

3.5   Discussion And Summary

In this chapter, we have studied numerically the linear elastic mechanical response of disc packings near jamming. The packings are subjected to both homogeneous strain and point forcing. We have also discussed the response of small subsystems to homogeneous strain subject to rigid, no slip boundaries. In the case of the point-like external force, while the continuum approach produces a simple scaling behavior for the Fourier components, the actual Green's function displays a strikingly different behavior; at small wavelengths the response shows a clear departure from the expectations the extent of which increases near jamming. The observed behavior identifies a crossover length whose location depends on the proximity to jamming.

For constrained homogeneous shear, we also identify a characteristic length associated with the size dependent average shear modulus. This length determines how quickly one recovers the underlying global shear constant for an unconstrained sample. We have shown that both lengths scale as an inverse power of the applied, global hydrostatic pressure, p.

Our results indicate that, in all cases, although the transverse component of the response is dominant, the longitudinal component shows much more sensitivity to the jamming transition. For the response to unconstrained homogeneous strain, we are unable to identify any simple scaling with p. However, surprisingly, we find agreement between the response to shear and compression: in both cases it is the longitudinal contribution that is sensitive to proximity to jamming. The physical picture that emerges is that zones of strong local shearing, which are present in the transverse response at *all p*

for both imposed shear and compression/dilation, can organize the dilatancy field at large length scales for large p, but are unable to do so at low p near jamming.

Chapter 4

Summary And Conclusions

The starting point of this thesis is a very simple question: in static particle packings, there are inherent spatial fluctuations and correlations in the quenched stress structure and local elastic properties; how far could the mechanical response of these particle assemblies be described simply by assuming that they are uniform in space? This is the essence of linear isotropic homogeneous elasticity.

To address this question, we began by studying local stress fluctuations; at first glance, the two-point force correlation function might seem sufficient to capture the interesting features of stress fluctuations. A careful investigation of this function in isotropically compressed packings led to correlation lengths of a few particles which are almost insensitive to jamming [30, 26]. The work of Henkes and Chakraborty(HC) [14, 15, 27] established a theoretical framework for describing the power spectrum of the stress field. If one has access to such a description, one may compute the strength of stress fluctuations in the coarse-grained field. Based on this strategy, in Chapter 2,

we provided a novel description of stress chains which is able to capture most of their interesting properties. We also found that the deviatoric magnitude of the coarse-grained field shows some remarkable features which are surprisingly close to those of the stress fluctuations. While our approach based on stress fluctuations is closely related to the HC's theory, its immediate relation to the stress anisotropy method remains subtle. The way we have analyzed our data here could lead to development of a new tool for the study of force chains, a problem so far tackled mostly by standard correlation functions. In principle, it should be straightforward to analyze stress fields obtained from experiments in much the same way.

With the clear emergence of strong inhomogeneities, linear elasticity looks too simplistic to describe the mechanical response in particle packings; its robustness and effectiveness must be discussed from the jamming transition perspective. In Chapter 3, we found length scales associated with the point response below which continuum approaches fail. The scaling laws proposed for these lengths at vanishing pressure display a form of critical behavior shown by several other studies [9, 7, 46].

There is still one big open question that should be kept in mind: what is the role of local quenched stresses in the linear elastic response of particle assemblies? Our results, altogether, suggest that stress correlations and local elastic properties of these systems share many common features. However, an important aspect which is still unclear is to what extent they can be predicted from one another.

Bibliography

[1] Rheology of foams and highly concentrated emulsions: Iii. static shear modulus. *Journal of Colloid and Interface Science*, 112(2):427 – 437, 1986.

[2] Roberto Arevalo, Iker Zuriguel, and Diego Maza. Topology of the force network in the jamming transition of an isotropically compressed granular packing. *PHYSICAL REVIEW E*, 81(4, Part 1), 2010.

[3] T H K Barron and M L Klein. Second-order elastic constants of a solid under stress. *Proceedings of the Physical Society*, 85(3):523, 1965.

[4] P A Cundall and O D L Strack. A discrete numerical model for granular assemblies. *Gotechnique*, 29(1):47–65, 1979.

[5] BA DiDonna and TC Lubensky. Nonaffine correlations in random elastic media. *PHYSICAL REVIEW E*, 72(6, 2), 2005.

[6] A. Drescher and Dejossel.G. Photoelastic verification of a mechanical model for the flow of a granular material. *Journal of the Mechanics and Physics of Solids*, 20(5):337–340, 1972.

[7] Gustavo Duering, Edan Lerner, and Matthieu Wyart. Phonon gap and localization lengths in floppy materials. *SOFT MATTER*, 9(1):146–154, 2013.

[8] S.F. Edwards and R.B.S. Oakeshott. Theory of powders. *Physica A: Statistical Mechanics and its Applications*, 157(3):1080 – 1090, 1989.

[9] W. G. Ellenbroek, Z. Zeravcic, W. van Saarloos, and M. van Hecke. Non-affine response: Jammed packings vs. spring networks. *EPL*, 87(3), 2009.

[10] Wouter G. Ellenbroek, Ellák Somfai, Martin van Hecke, and Wim van Saarloos. Critical scaling in linear response of frictionless granular packings near jamming. *Phys. Rev. Lett.*, 97:258001, 2006.

[11] Wouter G. Ellenbroek, Martin van Hecke, and Wim van Saarloos. Jammed frictionless disks: Connecting local and global response. *Phys. Rev. E*, 80:061307, 2009.

[12] J. F. Geng, D. Howell, E. Longhi, R. P. Behringer, G. Reydellet, L. Vanel, E. Clement, and S. Luding. Footprints in sand: The response of a granular material to local perturbations. *Physical Review Letters*, 87(3), 2001.

[13] Carl P. Goodrich, Wouter G. Ellenbroek, and Andrea J. Liu. Stability of jammed packings I: the rigidity length scale. *SOFT MATTER*, 9(46):10993–10999, 2013.

[14] Silke Henkes and Bulbul Chakraborty. Jamming as a critical phenomenon: A field theory of zero-temperature grain packings. *Phys. Rev. Lett.*, 95:198002, 2005.

[15] Silke Henkes and Bulbul Chakraborty. Statistical mechanics framework for static granular matter. *PHYSICAL REVIEW E*, 79(6), 2009.

[16] D. Howell, R. P. Behringer, and C. Veje. Stress fluctuations in a 2d granular couette experiment: A continuous transition. *Physical Review Letters*, 82(26):5241–5244, 1999.

[17] X. Jia, C. Caroli, and B. Velicky. Ultrasound propagation in externally stressed granular media. *Physical Review Letters*, 82(9):1863–1866, 1999.

[18] L. Kondic, A. Goullet, C. S. O'Hern, M. Kramar, K. Mischaikow, and R. P. Behringer. Topology of force networks in compressed granular media. *EPL*, 97(5), 2012.

[19] Martin-D. Lacasse, Gary S. Grest, Dov Levine, T. G. Mason, and D. A. Weitz. Model for the elasticity of compressed emulsions. *Phys. Rev. Lett.*, 76:3448–3451, 1996.

[20] A Lemaitre and C Maloney. Sum rules for the quasi-static and visco-elastic response of disordered solids at zero temperature. *Journal of Statistical Physics*, 123(2):415–453, 2006.

[21] F. Leonforte, R. Boissiere, A. Tanguy, J. P. Wittmer, and J. L. Barrat. Continuum limit of amorphous elastic bodies. iii. three-dimensional systems. *Physical Review B*, 72(22), 2005.

[22] F. Leonforte, A. Tanguy, J. P. Wittmer, and J. L. Barrat. Continuum limit of amorphous elastic bodies ii: Linear response to a point source force. *Physical Review B*, 70(1), 2004.

[23] F. Leonforte, A. Tanguy, J. P. Wittmer, and J.-L. Barrat. Inhomogeneous elastic response of silica glass. *Phys. Rev. Lett.*, 97:055501, 2006.

[24] AJ Liu and SR Nagel. Nonlinear dynamics - Jamming is not just cool any more. *NATURE*, 396(6706):21–22, 1998.

[25] C. h. Liu, S. R. Nagel, D. A. Schecter, S. N. Coppersmith, S. Majumdar, O. Narayan, and T. A. Witten. Force fluctuations in bead packs. *Science*, 269(5223):513–515, 1995.

[26] G. Lois, J. Zhang, T. S. Majmudar, S. Henkes, B. Chakraborty, C. S. O'Hern, and R. P. Behringer. Stress correlations in granular materials: An entropic formulation. *Phys. Rev. E*, 80:060303, 2009.

[27] G. Lois, J. Zhang, T. S. Majmudar, S. Henkes, B. Chakraborty, C. S. O'Hern, and R. P. Behringer. Stress correlations in granular materials: An entropic formulation. *Phys. Rev. E*, 80:060303, 2009.

[28] G Lovoll, KJ Maloy, and EG Flekkoy. Force measurements on static granular materials. *Physical Review E*, 60(5, Part b):5872–5878, 1999.

[29] D. J. Tildesley M. P. Allen. *Computer Simulation of Liquids*. Oxford University Press, Oxford, 1989.

[30] TS Majmudar and RP Behringer. Contact force measurements and stress-induced anisotropy in granular materials. *NATURE*, 435(7045):1079–1082, 2005.

[31] HA Makse, N Gland, DL Johnson, and LM Schwartz. Why effective medium theory fails in granular materials. *PHYSICAL REVIEW LETTERS*, 83(24):5070–5073, 1999.

[32] HA Makse, DL Johnson, and LM Schwartz. Packing of compressible granular materials. *Physical Review Letters*, 84(18):4160–4163, 2000.

[33] C. E. Maloney. Correlations in the elastic response of dense random packings. *Phys. Rev. Lett.*, 97:035503, 2006.

[34] T. G. Mason, J. Bibette, and D. A. Weitz. Elasticity of compressed emulsions. *Phys. Rev. Lett.*, 75:2051–2054, 1995.

[35] T. G. Mason, J. Bibette, and D. A. Weitz. Elasticity of compressed emulsions. *Phys. Rev. Lett.*, 75:2051–2054, 1995.

[36] T. G. Mason, Martin-D. Lacasse, Gary S. Grest, Dov Levine, J. Bibette, and D. A. Weitz. Osmotic pressure and viscoelastic shear moduli of concentrated emulsions. *Phys. Rev. E*, 56:3150–3166, 1997.

[37] Hideyuki Mizuno, Stefano Mossa, and Jean-Louis Barrat. Measuring spatial distribution of the local elastic modulus in glasses. *PHYSICAL REVIEW E*, 87(4), 2013.

[38] DM Mueth, HM Jaeger, and SR Nagel. Force distribution in a granular medium. *Physical Review E*, 57(3, Part b):3164–3169, 1998.

[39] Micha-Klaus Muller, Stefan Luding, and Thorsten Poeschel. Force statistics and correlations in dense granular packings. *Chemical Physics*, 375(2-3):600–605, 2010.

[40] Corey S. O'Hern, Leonardo E. Silbert, Andrea J. Liu, and Sidney R. Nagel. Jamming at zero temperature and zero applied stress: The epitome of disorder. *Phys. Rev. E*, 68:011306, 2003.

[41] S Ostojic, E Somfai, and B Nienhuis. Scale invariance and universality of force networks in static granular matter. *Nature*, 439(7078):828–830, 2006.

[42] Steve Plimpton. Fast parallel algorithms for short-range molecular dynamics. *Journal of Computational Physics*, 117(1):1 – 19, 1995.

[43] F Radjai, M Jean, JJ Moreau, and S Roux. Force distributions in dense two-dimensional granular systems. *PHYSICAL REVIEW LETTERS*, 77(2):274–277, 1996.

[44] Samuel S. Schoenholz, Carl P. Goodrich, Oleg Kogan, Andrea J. Liu, and Sidney R. Nagel. Stability of jammed packings II: the transverse length scale. *SOFT MATTER*, 9(46):11000–11006, 2013.

[45] LE Silbert, GS Grest, and JW Landry. Statistics of the contact network in frictional and frictionless granular packings. *PHYSICAL REVIEW E*, 66(6, 1), 2002.

[46] LE Silbert, AJ Liu, and SR Nagel. Vibrations and diverging length scales near the unjamming transition. *PHYSICAL REVIEW LETTERS*, 95(9), 2005.

[47] JH Snoeijer, TJH Vlugt, M van Hecke, and W van Saarloos. Force network ensemble: A new approach to static granular matter. *Physical Review Letters* , 92(5), 2004.

[48] A. Tanguy, J. P. Wittmer, F. Leonforte, and J. L. Barrat. Continuum limit of amorphous elastic bodies: A finite-size study of low-frequency harmonic vibrations. *Physical Review B*, 66(17), 2002.

[49] Brian P. Tighe and Thijs J. H. Vlugt. Stress fluctuations in granular force networks. *JOURNAL OF STATISTICAL MECHANICS-THEORY AND EXPERIMENT*, 2011.

[50] Michel Tsamados, Anne Tanguy, Chay Goldenberg, and Jean-Louis Barrat. Local elasticity map and plasticity in a model lennard-jones glass. *Physical Review E*, 80(2), 2009.

[51] M. van Hecke. Jamming of soft particles: geometry, mechanics, scaling and isostaticity. *JOURNAL OF PHYSICS-CONDENSED MATTER*, 22(3), 2010.

[52] M Wyart, SR Nagel, and TA Witten. Geometric origin of excess low-frequency vibrational modes in weakly connected amorphous solids. *EUROPHYSICS LETTERS*, 72(3):486–492, 2005.

[53] M Wyart, LE Silbert, SR Nagel, and TA Witten. Effects of compression on the vibrational modes of marginally jammed solids. *PHYSICAL REVIEW E*, 72(5, 1), 2005.

[54] N. Xu, V. Vitelli, A. J. Liu, and S. R. Nagel. Anharmonic and quasi-localized vibrations in jammed solids-Modes for mechanical failure. *EPL*, 90(5), 2010.

[55] K Yoshimoto, TS Jain, KV Workum, PF Nealey, and JJ de Pablo. Mechanical heterogeneities in model polymer glasses at small length scales. *Physical Review Letters*, 93(17), 2004.

Appendices
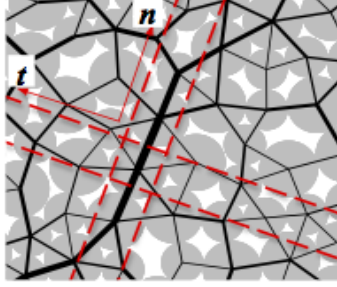
Appendix A

Stress Correlations

Figure A.1: Illustration of the principal stress axes (n_α and t_α) for an arbitrary particle.

A.1   Anisotropic Correlation Function

As discussed in the text, the force network exhibits strong local anisotropy down to a few particle size scale, even under uniform compression. More insight about the force structure can be gained by studying a modified correlation function that determines correlations along *locally determined* principal stress directions. The new anisotropic analysis only incorporates pairs of particles that lie within the illustrated boxes in Fig. A.1. For each particle, these boxes are aligned with principal stress directions that are determined from the virial stress tensor. In that case, the anisotropic correlation function is defined as

$$G^{\text{mod}}(R) = \frac{\langle p_o p_r \rangle - \langle p_o \rangle \langle p_r \rangle}{\sigma_{p_o} \sigma_{p_r}}, \tag{A.1}$$

where "o" is the particle at the origin and "r" is the remote particle and

$$\langle p_o p_r \rangle = \frac{1}{M} \sum_{i=1}^{N} \sum_{j=1}^{N} \delta(R n_{i\alpha} - r_{ij\alpha}) p_i p_j, \tag{A.2}$$

$$\langle p_o \rangle = \frac{1}{M} \sum_{i=1}^{N} \sum_{j=1}^{N} \delta(Rn_{i\alpha} - r_{ij\alpha})p_i, \tag{A.3}$$

$$\langle p_r \rangle = \frac{1}{M} \sum_{i=1}^{N} \sum_{j=1}^{N} \delta(Rn_{i\alpha} - r_{ij\alpha})p_j, \tag{A.4}$$

$$\sigma_{p_o}^2 = \frac{1}{M} \sum_{i=1}^{N} \sum_{j=1}^{N} \delta(Rn_{i\alpha} - r_{ij\alpha})p_i^2 - \langle p_o \rangle^2, \tag{A.5}$$

$$\sigma_{p_r}^2 = \frac{1}{M} \sum_{i=1}^{N} \sum_{j=1}^{N} \delta(Rn_{i\alpha} - r_{ij\alpha})p_j^2 - \langle p_r \rangle^2, \tag{A.6}$$

, and

$$M = \sum_{i=1}^{N} \sum_{j=1}^{N} \delta(Rn_{i\alpha} - r_{ij\alpha}). \tag{A.7}$$

Here, $n_{i\alpha}$ is a unit vector along the major principal stress axis, which is computed from the virial of particle i, pointing from particle i to j. Note that in the conventional correlation function pair ij is treated the same as pair ji, whereas the anisotropic case considers both the separation and the direction. Pairs do not come symmetricaly in this modified calculation: if particle j lies along $n_{i\alpha}$, particle i does not necessarily lie along $n_{j\alpha}$. In general $n_{i\alpha} \neq n_{j\alpha}$. Consequently, $\langle p_o \rangle \neq \langle p_r \rangle$ and $\sigma_{p_o} \neq \sigma_{p_r}$. A similar correlation function may be computed for the minor principal stress axis.

Appendix B

Elasticity

B.1 Bulk Elastic Constants

Let us now derive microscopic equations for the stress and elastic constants, quantities typically defined from continuum mechanics. Because of the non-affine displacements, the strain-energy density is now a function of $\delta u_{i\alpha}$ too. Using Eqs. (3.1) and (3.11) we have

$$(\mathcal{U} - \mathcal{U}_0)/V \approx \mathring{\sigma}_{\alpha\beta}\eta_{\alpha\beta} + \frac{1}{2}\eta_{\alpha\beta}C_{\alpha\beta\gamma\delta}\eta_{\gamma\delta}, \tag{B.1}$$

where $C_{\alpha\beta\gamma\delta} = C_{\alpha\beta\gamma\delta}^{\text{Born}} - \frac{1}{V}\Xi_{i\sigma\alpha\beta}H_{i\sigma j\tau}^{-1}\Xi_{j\tau\gamma\delta}$ and $\mathring{\sigma}_{\alpha\beta} = \frac{1}{V}\partial\mathcal{U}/\partial\eta_{\alpha\beta}$. The Born approximation $C_{\alpha\beta\gamma\delta}^{\text{Born}}$ for the second derivative of the energy with respect to $\eta_{\alpha\beta}$ corresponds to strictly affine displacements of the particles. The contraction of the inverse of the Hessian on components of $\Xi_{i\alpha\beta\gamma}$ provide the correction terms. Since $H_{i\alpha j\beta}^{-1}$ is positive definite, the correction terms are positive: That is, non-affine displacements reduce the second order derivative of the energy from its Born form ($C_{\alpha\beta\gamma\delta} \leq C_{\alpha\beta\gamma\delta}^{\text{Born}}$ when $\alpha\beta = \gamma\delta$).

In a system with pair-wise interactions potential, the Born estimates may be computed by carrying out a simple summation over all pairs of interacting particles (see [20])

$$C_{\alpha\beta\gamma\delta}^{\text{Born}} = \frac{1}{V}\sum_{ij}(r_{ij}U''(r_{ij}) - U'(r_{ij}))r_{ij}n_{ij}^{\alpha}n_{ij}^{\beta}n_{ij}^{\delta}n_{ij}^{\gamma}, \tag{B.2}$$

where we have introduced the normalized vector between pairs of particles $n_{ij}^{\alpha} = r_{ij}^{\alpha}/r_{ij}$. And for the fields $\Xi_{i\alpha\beta\gamma}$, the derived expression is

$$\Xi_{i\alpha\beta\gamma} = -\sum_{j}(r_{ij}U''(r_{ij}) - U'(r_{ij}))n_{ij}^{\alpha}n_{ij}^{\beta}n_{ij}^{\gamma}. \tag{B.3}$$

Now we are ready to calculate $C_{\alpha\beta\gamma\delta}$ from numerical samples. Since we are dealing with large system sizes, we can expect that the elasticity tensor is almost isotropic and it has a form very close to $C^{\mathcal{L}}_{\alpha\beta\gamma\delta}$ (see Appendix B.3). The two modes of deformation that we need to use here are isotropic compression $\eta_{\alpha\beta} = \epsilon\delta_{\alpha\beta}$ and pure shear $\eta_{\alpha\beta} = \epsilon(\delta_{\alpha x}\delta_{\beta x} - \delta_{\alpha y}\delta_{\beta y})$ where ϵ is an infinitesimal strain. Given these modes of deformation, we are able to make a direct measurements of $K = \frac{1}{4}(C_{xxxx}+C_{yyyy}+2C_{xxyy})$ and $\mu = \frac{1}{4}(C_{xxxx}+C_{yyyy}-2C_{xxyy})$.

B.2 Plane Wave Procedure

The expansion of the energy in terms of $\eta_{\alpha,\beta}$ is written

$$(\mathcal{U} - \mathcal{U}_0) \approx \int (\mathring{\sigma}_{\alpha\beta}\eta_{\alpha\beta} + \frac{1}{2}\eta_{\alpha\beta}C_{\alpha\beta\gamma\delta}\eta_{\gamma\delta})dV, \tag{B.4}$$

where $2\eta_{\alpha\beta} = \partial_\beta u_\alpha + \partial_\alpha u_\beta + \partial_\alpha u_\gamma \partial_\beta u_\gamma$. Inserting the Fourier expansion of Eq. (B.12) into the above equation reads and using $C_{\alpha\beta\gamma\delta} = C^{\mathcal{L}}_{\alpha\beta\gamma\delta}$ and $\mathring{\sigma}_{\alpha\beta} = -p\delta_{\alpha\beta}$, we obtain

$$\begin{aligned}
(\mathcal{U} - \mathcal{U}_0)/V &\approx K \sum_{\mathbf{q}} q^2 |u_L(\mathbf{q})|^2 \\
&+ (\mu - p) \sum_{\mathbf{q}} q^2 (|u_L(\mathbf{q})|^2 + |u_T(\mathbf{q})|^2).
\end{aligned} \tag{B.5}$$

Now let us derive $u_L(\mathbf{q})$ and $u_T(\mathbf{q})$ for a transverse plane wave perturbation (with wave vector $\mathbf{q}'$) and substitute in the above equation. We have

$$\begin{aligned}
f_L(\mathbf{x}) &= 0, \\
f_T(\mathbf{x}) &= \frac{F}{\sqrt{N}} \sum_j \delta(\mathbf{x} - \mathbf{x}_j) e^{i\mathbf{q}'.\mathbf{x}_j},
\end{aligned} \tag{B.6}$$

Hence,

$$\begin{aligned}
f_L(\mathbf{q}) &= 0, \\
f_T(\mathbf{q}) &= \frac{F}{V}\sqrt{N}\delta_{\mathbf{q},\mathbf{q}'}.
\end{aligned} \tag{B.7}$$

where $\delta_{\mathbf{q,q'}}$ is a Kronecker delta. Using Eq. (B.14) leads us to

$$
\begin{aligned}
u_L(\mathbf{q}) &= 0, \\
u_T(\mathbf{q}) &= \frac{F}{V}\sqrt{N}\delta_{\mathbf{q,q'}}/\mu q^2,
\end{aligned}
\tag{B.8}
$$

And by inserting them in Eq. (B.5), the energy can be expressed as

$$
\mathcal{U} - \mathcal{U}_0 \approx F^2[(\mu - \langle p \rangle)q'^2 V/N]^{-1},
\tag{B.9}
$$

where the entire term in the parenthesis has unit of stiffness. We may now calculate $\mathcal{U} - \mathcal{U}_0$ from Section 3.3.2 as the elastic energy of an *atomistic* system and use it to obtain μ.

B.3 Linear Isotropic Elasticity

The continuum solution $u_\alpha(\mathbf{x})$ is obtained from the equations of motion in terms of the $C_{\alpha\beta\gamma\delta}$ given by [3]

$$(C_{\alpha\beta\gamma\delta} + \mathring{\sigma}_{\beta\delta}\delta_{\alpha\gamma})\partial_\beta\partial_\delta u_\gamma = -f_\alpha, \tag{B.10}$$

with f_α being the external body force. We assume that the continuum medium is homogeneous, isotropic, and linearly elastic. The elastic properties of the medium are fully described by the Lamé constants λ and μ, i.e. $C^{\mathcal{L}}_{\alpha\beta\gamma\delta} = \lambda\delta_{\alpha\beta}\delta_{\gamma\delta} + \mu(\delta_{\alpha\delta}\delta_{\beta\gamma} + \delta_{\alpha\gamma}\delta_{\beta\delta})$. Let us also assume that a uniform isotropic initial stress in the reference state is defined by $\mathring{\sigma}_{\alpha\beta} = -p\delta_{\alpha\beta}$ where p is the pressure. Substituting those expressions into Eq. (B.10) yields

$$(\mu - p)\, u_{\alpha,\beta\beta} + K\,\partial_\beta\partial_\alpha u_\beta = -f_\alpha, \tag{B.11}$$

where $K = \lambda + \mu$ (in $2D$) is the bulk modulus. For a square packing of size L with periodic boundaries along x and y, Eq. (B.11) can be solved in terms of a Fourier series

$$u_\alpha(\mathbf{x}) = \sum_{\mathbf{q}} u_\alpha(\mathbf{q})\, e^{i\mathbf{q}\cdot\mathbf{x}}. \tag{B.12}$$

Inserting the expansions into Eq. (B.11), $\hat{u}_\alpha(\mathbf{q})$ is most simply displayed as

$$[(\mu - p)\delta_{\alpha\beta} + Kn_\alpha n_\beta]\, u_\beta(\mathbf{q}) = \frac{1}{q^2} f_\alpha(\mathbf{q}), \tag{B.13}$$

where $q^2 = q_\alpha q_\alpha$, $n_\alpha = q_\alpha/q$, and $f_\alpha(\mathbf{q}) = \frac{1}{V}\int f_\alpha(\mathbf{x})\, e^{-i\mathbf{q}\cdot\mathbf{x}}dV$.

Given that the longitudinal and transverse waves are the eigenmodes of

the Lame-Navier operator – the second order tensor in brackets in Eq. (B.13)–, the longitudinal and transverse components of $u_\alpha(\mathbf{q})$ are

$$
\begin{aligned}
u_L^{\text{cont}}(\mathbf{q}) &= \frac{f_L(\mathbf{q})}{(K+\mu)q^2}, \\
u_T^{\text{cont}}(\mathbf{q}) &= \frac{f_T(\mathbf{q})}{\mu q^2},
\end{aligned}
\tag{B.14}
$$

where $f_L(\mathbf{q})$ and $f_T(\mathbf{q})$ are the longitudinal and transverse components of $f_\alpha(\mathbf{q})$, i.e. $f_\alpha(\mathbf{q}) = f_L(\mathbf{q})n_\alpha + f_T(\mathbf{q})n_\alpha^\perp$. For a vertical point force of the form $\mathbf{f}(\mathbf{x}) = -F\delta(\mathbf{x})\hat{y}$, the longitudinal and transverse components become

$$
\begin{aligned}
f_L(\mathbf{q}) &= \frac{F}{V}\sin(\theta), \\
f_T(\mathbf{q}) &= \frac{F}{V}\cos(\theta),
\end{aligned}
\tag{B.15}
$$

where $\delta(\mathbf{x})$ is a delta function, $\hat{y}$ is a unit cartesian vector along y, F is the force magnitude, and θ is the angle of $\mathbf{q}$.

Inserting Eq. (B.15) in Eq. (B.14) yields

$$
\begin{aligned}
u_L^{\text{cont}}(\mathbf{q}) &= \frac{F\,\sin(\theta)}{(K+\mu)q^2\,V}, \\
u_T^{\text{cont}}(\mathbf{q}) &= \frac{F\,\cos(\theta)}{\mu q^2\,V}.
\end{aligned}
\tag{B.16}
$$

See Appendix B.1 where we derive an expression for K and μ.